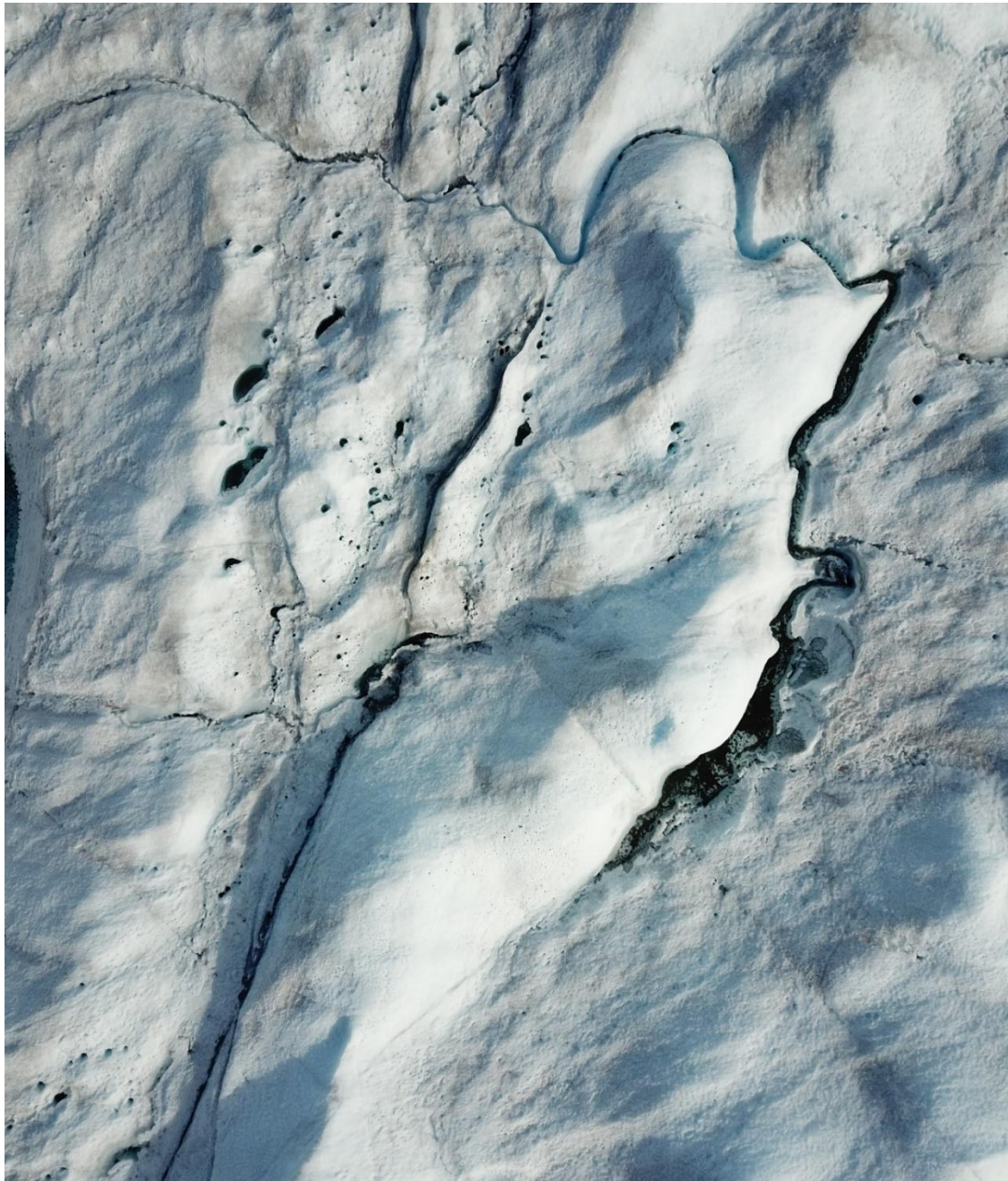# Estimating aerodynamic roughness using different topographic methods for the Greenland Ice Sheet using RPAS photogrammetry

MSc Thesis

Supervisors: W. W. Immerzeel, J. F. Steiner, M. van Tiggelen

E. J. Nieuwstraten – Universiteit Utrecht – 563020 – e.j.nieuwstraten@uu.nl

Table of contents

Abstract

Remotely Piloted Aircraft Systems (RPAS) have become an important tool in studying glaciers and their surfaces as they can generate high-resolution ortho-images and digital elevation models (DEM). It is important to monitor the surface of the Greenland Ice Sheet (GrIS) as it has become the largest cryospheric contributor to sea-level rise. Glacier surface energy balance models can provide insight in the mass loss rate and show that turbulent fluxes can form a major component. Aerodynamic roughness is an important parameter in these models, for which currently a fixed value is often used. This paper therefore analyses the possibilities of using RPAS-derived DEMs to quantify topographic roughness and its impact on turbulent energy fluxes on the GrIS. To answer this question, the following two unique methods were developed. First, the Moving Footprint (MF) method which produces a roughness estimate for a single location by moving a rotating footprint of varying size over the DEM. This footprint then extracts transects to which commonly used microtopographic algorithms (Lettau, Munro, and Nield) were applied. Second, the Fixed Grid (FG) method which produces a distribution of roughness values over the study area, by subdividing the study area in grid cells in which commonly used microtopographic algorithms (Lettau, Munro, and Nield) were applied. Our results show that both methods can produce realistic roughness estimates for a range of scales using certain algorithms. In the MF method, the Lettau algorithm performs well, while in the FG method, the Munro, Nield SdElev and Nield Max algorithms perform well. Moreover, we prove that the simulated sensible heat fluxes using roughness values derived using the MF method (Lettau, 5x40m footprint) or FG method (Munro, Nield SdElev, 5m grid size) are as accurate as simulated sensible heat fluxes using roughness values obtained by aerodynamic inversion of automatic weather station (AWS) data. The implication of these findings are that RPAS surveys are capable of producing realistic estimates of topographic roughness when using the methodology developed in this study, and thus contribute to the improvement of turbulent energy flux estimations for areas on the GrIS where no AWS are present.

1. Introduction

1.1 Background

1.1.1 Introduction on Greenland Ice Sheet

The Greenland Ice Sheet (GrIS) has become the largest cryospheric contributor to global sea-level rise as a result of both increased surface melt and runoff as well as increased ice discharge from marine-terminating outlet glaciers (Enderlin et al., 2014; Sasgen et al., 2012). During the first decade of the 21st century, mass loss of the GrIS was composed of surface melting which results in runoff, and ice discharge from marine-terminating glaciers in approximately equal parts (van den Broeke et al., 2009). During the period 2009-2014, 84% of the increase in rate of mass loss has been due to increased surface melting and runoff (Enderlin et al., 2014), implying that surface melt is the primary driver of GrIS mass loss on decadal and greater time scales (Nick et al., 2013; Wouters et al., 2013). It was expected that the surface melt of the GrIS would continue to accelerate with ongoing climate change (Fettweis et al., 2013). However, recent research illustrated the difficulty of extrapolating short records into longer-term trends as cold summers in 2010-2018 caused the surface melt to decelerate (Mouginot et al., 2019). Nevertheless, an average of 0.69 mm yr^{-1} sea level rise contribution during the 2012-2016 period is observed (Bamber et al., 2018; Bevis et al., 2019). Thus, while the acceleration may be negative, it is expected that due to ongoing climate change substantial fresh water fluxes will be originating from the GrIS as the mass loss is increasing (Fettweis et al., 2013). Understanding the mass loss rate of the GrIS is of great importance due to the potential implications of this large freshwater influx into the surrounding oceans (Böning et al., 2016), next to Greenland's large contribution to current (van den Broeke et al., 2016) and expected future sea level rise (Cuffey and Marshall, 2000). One way to better understand the mass loss rate is to apply glacier surface energy balance models (Hock, 2005). It is shown that in these surface energy balance models, turbulent fluxes of sensible and latent heat can form a major component and substantially influence its rate of surface melt (Fitzpatrick et al., 2019). The bulk aerodynamic method is commonly used to parametrise the turbulent fluxes. This requires the input of roughness length values, and therefore is aerodynamic roughness an important parameter for these glacier surface energy balance models (Smeets and van den Broeke, 2008).

1.1.2 Introduction on surface and aerodynamic roughness

Roughness is a widely used term in Earth Sciences (Smith, 2014). While the term 'roughness' is used ambiguously, it is mostly used to describe sub-grid scale topography, which in the following is referred to as 'surface roughness' (Smith, 2014). The notion of sub-grid scale topography induces one characteristic of surface roughness, namely its scale-dependency. It is key to refer to some grid scale that acts to partition roughness and topography. Therefore, an upper and lower limit should be defined for the analysis of surface roughness. Below the lower boundary, the measurement scale, topographic variations are unknown, or are indistinguishable from instrument error. Above the upper boundary, the partition scale, topographic variability is represented explicitly. Between the upper and lower boundary, it is parametrised as surface roughness. Advances in surveying techniques have increased the range of scales over which the roughness-topography partition has been applied, ranging from magnitudes of 0.1 m (Nield et al., 2011) to 50 km (Smith, Raymond, and Scambos, 2006). Quantifying the surface roughness value as the partition scale provides useful insights in the scale-dependency of roughness. A useful reference point is the scale at which this relationship changes, also known as the interface width (Figure 1).
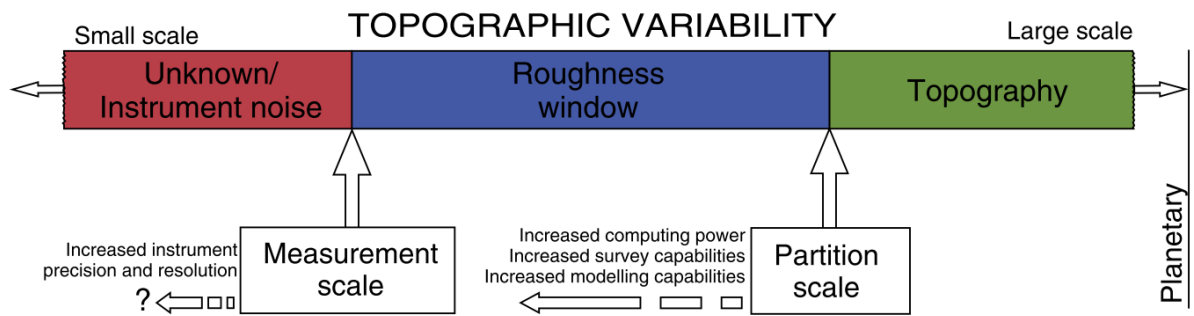
Figure 1. Schematic outline of the relationship between the measurement and partition scales and roughness measurement (Smith, 2014)

A prerequisite for many procedures of quantifying surface roughness, is filtering out overall topographic trends. Surfaces are often detrended using a variety of methods including (bi)linearly detrending e.g. (Miles et al., 2017), second-order polynomials e.g. (Rodríguez-Caballero et al., 2012) or median filtering (Hiller and Smith, 2008). Both the method of detrending and the scale of which it is applied are of great relevance to roughness parameterisations. For example, high-order polynomials approximate the real surface variability more closely, reducing the amount of overall roughness. In contrary, linear detrending will cause areas of high curvature to be represented as higher roughness values (Haubrock et al., 2009). This is illustrated in Figure 2 (Glenn et al., 2006).
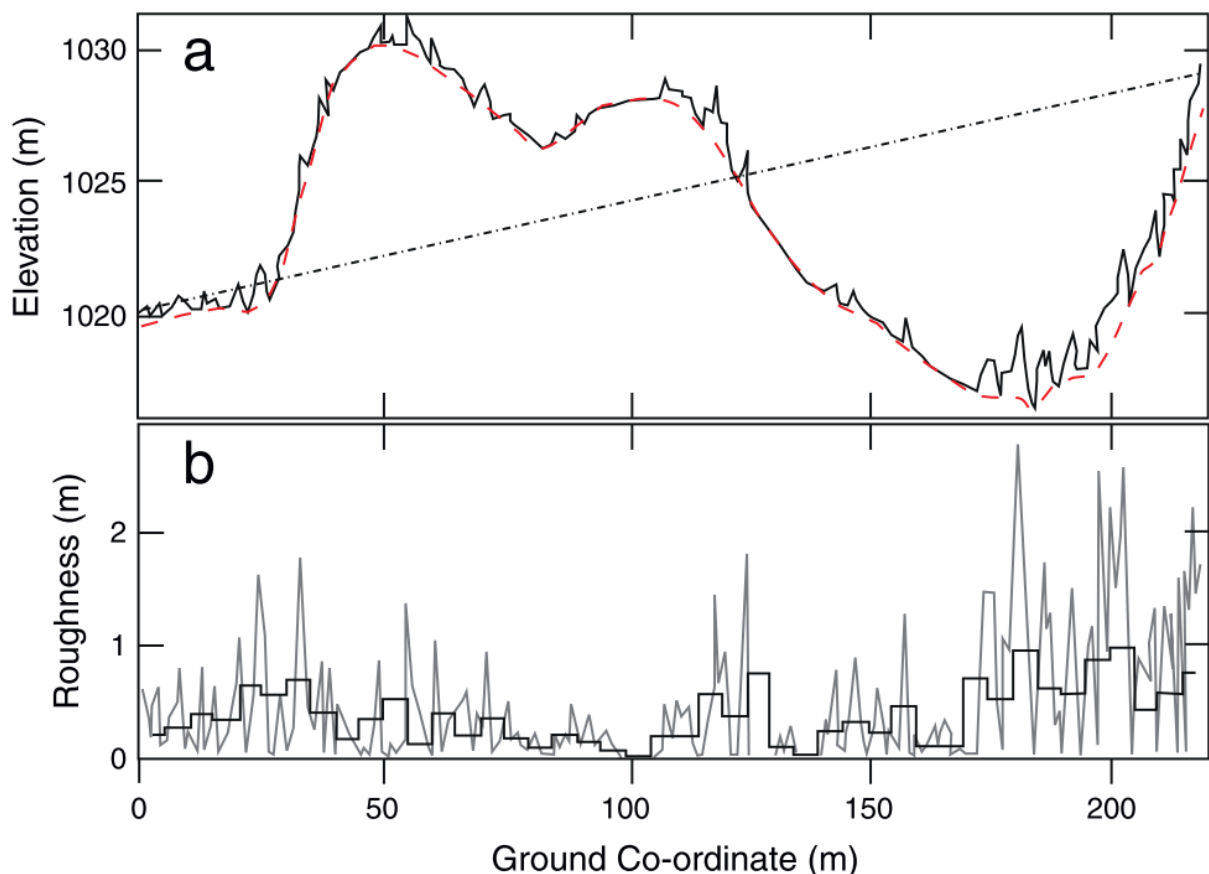
Figure 2. (a) Detrending a one-dimensional elevation profile (LiDAR derived, 1m resolution, solid line) using a thin-plate spline interpolated underlying surface (dashed) or simple linear interpolation over the whole baseline (dot-dash); (b) aggregation of LiDAR roughness (defined as the standard deviation of residuals from thin-plate spline in (a), grey line) into 5 m cells (black line). After Glenn et al. (2006: p.135).

Surface roughness is often applied as a surrogate for other variables that are more difficult to retrieve directly. One of these variables is the aerodynamic roughness length (in the following referred to as 'aerodynamic roughness' or simply z_0). The aerodynamic roughness length is defined as the length scale that characterises the loss of flow momentum attributable to surface roughness (Chappell and Heritage, 2007). Simply, it is the height above the ground surface where the inertial semi-logarithmic wind profile extrapolates to zero. As such, it is a parameter that controls the loss of momentum by turbulent transfer. Although z_0 and surface roughness are fundamentally different, relationships between z_0 and microtopography are commonly exploited to obtain z_0 values (Nield et al., 2013; Smith, 2014; Smith et al., 2016). Empirical relationships probably represent actual values of z_0 best, as they are developed from paired wind and topographic measurements. Many recently developed methods are not empirically derived, but are mechanical approximations which may be a significant shortcoming (e.g. Irvine-Fynn et al., 2014; Rounce, Quincey, and McKinney, 2015). By definition, z_0 directly influences the turbulent exchange of sensible and latent energy at a surface, and is thus a crucial parameter in energy balance models (Brock et al., 2006, 2000). Moreover, uncertainty in z_0 values present a serious challenge in energy balance models since a change in order of magnitude of z_0 leads to an approximate factor of 2 change in estimated turbulent fluxes (Brock et al., 2010; Hock and Holmgren, 1996; Munro, 1989). Often, these fluxes are calculated with the bulk aerodynamic method in which z_0 is one of the key input parameters (Smeets and van den Broeke, 2008). A schematic representation of z_0 is given in Figure 3A, and how the AWS measurements are performed in Figure 3B.
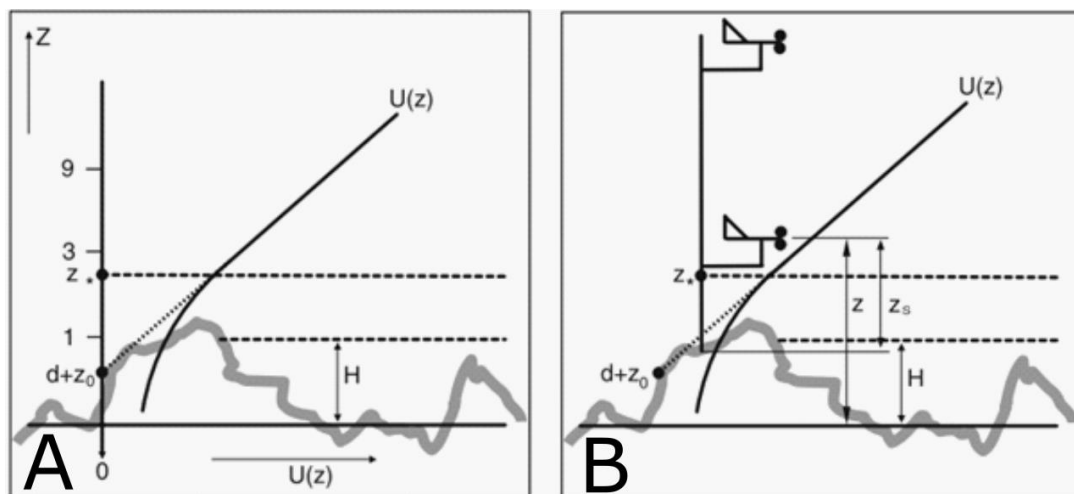
Figure 3. Schematic representations of (a) wind profile characteristics at a certain site with a rough-ice surface and (b) an automatic weather station (AWS) at this site (Smeets and van den Broeke, 2008). *In this figure U(z) is the average wind speed (m/s) as a function of height* z (m), d (m) is the zero-plane displacement, z_0 (m) is the aerodynamic roughness length, z_* (m) is the height of the roughness sublayer, z_s (m) the sensor height and H (m) is the average hummock height.

1.1.3 Remote sensing on the Greenland Ice Sheet

The first remote sensing data on the GrIS for civilian use date as far back as the mid-1960s, when images collected by the Nimbus satellite covered the GrIS (Bindschadler, 1998). Ever since, an increasing variety of sensors have been launched to monitor the earth and its ice sheets from space (Belward and Skøien, 2015). In recent years, a rapid increase in the number and range of earth observing satellites is occurring (Belward and Skøien, 2015). Key satellite remote sensing techniques next to optical imagery are radar altimetry, laser altimetry, gravimetry, multispectral optical imagery, and microwave and thermal imagery (Cooper and Smith, 2019). The new satellites are often capable of producing images of high spatial and temporal resolution (Cooper and Smith, 2019). Applications

are diverse, from the global land ice contribution to SLR during the satellite era (Bamber et al., 2018) to satellite remote sensing of polar climate change (Hall, 1988). Nevertheless, the temporal resolution and availability of very high spatial resolution satellite sensors (less than 10 m) are often still inadequate for many quantitative remote sensing applications (Manfreda et al., 2018). Furthermore, obtaining cloud-free data is complicated for all satellite sensors that do not operate in microwave wavelengths (Bhardwaj et al., 2016). Analysis of meteorological data has shown that optical satellite imagery in a rainy regions (yearly precipitation > 800mm) has a 20% probability of producing an adequate image (van der Wal et al., 2013). Most satellites that do provide high spatial and temporal resolution (e.g. CubeSat; (McCabe et al., 2017)) are operated by commercial organizations, causing the cost of image acquisition to become a limiting factor in studies where short revisit times are required (Manfreda et al., 2018).

Remotely Piloted Aircraft Systems (RPAS) prove to be of great use in this case, as they provide data of unprecedented spatial and temporal resolution at relative low cost (Bhardwaj et al., 2016). Additionally, RPAS-mounted sensors have two other key advantages. First, their ability to acquire data on specific dates or at a specific time is a major advantage over space-borne remote sensors (Bhardwaj et al., 2016; Manfreda et al., 2018). Second, RPAS are capable of collecting data under cloudy conditions during which satellite are not (always) capable of producing adequate images (van der Wal et al., 2013). Applications of RPAS are diverse, and range from research purposes such as mapping vegetation properties (Lu et al., 2018) to more applied purposes such as power line inspections (Teng et al., 2017).

A recent development in the field of RPAS-derived photogrammetry is the use of Global Navigation Satellite System-supported aerial triangulation (GNSS-AT; (Benassi et al., 2017)), which significantly reduces the need for Ground Control Points (GCPs) (Chudley et al., 2019). This technique makes use of differential carrier-phase GNSS positioning to accurately geolocate imagery and subsequent photogrammetric products (Benassi et al., 2017). This development is of great importance in e.g. the field of applied glaciology, in which producing a GCP network of adequate density is often not feasible due to impracticality, costs, and hazardous terrain (e.g. crevasses, moving icebergs) (Chudley et al., 2019). Other methods for overcoming the difficulties in building GCP networks include using tie points to tie datasets together geodetically (Kraaijenbrink et al., 2016), linearly interpolating the on-ice GCP location from the start and end point of a RPAS mission (Jouvet et al., 2017), or using an on-board navigational GPS geolocation (Ryan et al., 2015).

Through these developments, RPAS photogrammetry has become an important tool to study glaciers and their dynamics, as they are capable of generating multi-temporal, high resolution digital elevation models (DEMs) in the order of centimetre magnitude (Jouvet et al., 2019). These high resolution DEMs can be used to extract parameters used in the estimation of z_0 as is described in the section 2.5-2.7.

1.1.4 The importance of turbulent fluxes

Turbulent fluxes of sensible and latent heat are commonly considered to be secondary to radiative fluxes in glacier surface energy balance models (Hock, 2005). However, these turbulent fluxes over ice surfaces may be subject to systematic underestimation in Regional Climate Models (RCMs) (Elvidge et al., 2016; Noël et al., 2015). Furthermore, during overcast and windy conditions the turbulent fluxes of sensible and latent heat increase in significance (Giesen et al., 2014). These conditions are expected to become more frequent in a future, warming climate, therefore increasing the future significance of the nonradiative fluxes (Gorter et al., 2014; Schuenemann and Cassano, 2010; Vavrus, 2013). In the past, the nonradiative fluxes have contributed significantly to extreme melt events as was the case e.g. in the year 2012 (Fausto et al., 2016; Neff et al., 2014). On July 12th of 2012, satellite observations indicated that more than 98% of the GrIS surface was melting, a value unprecedented in the satellite

era (Nghiem et al., 2012). These melt events can often be correlated to the North Atlantic Oscillation (NAO) index. This index represents the pressure difference between the climatological high pressure system near the Azores, and the low pressure system near Iceland (Hurrell et al., 2003). A positive NAO index implies north-westerly flow over Arctic Greenland. A negative NAO index inverts this flow, resulting in earlier described advection of relatively warm air from southern latitudes to the GrIS (van Angelen et al., 2014). The warm air advected causes a large air-surface temperature gradient and as a result a significant role for the sensible heat flux as melt energy source. Some papers dispute the dominant role of the NAO, suggesting an alternative dominant position for the Arctic Dipole in relation to large-scale melt (Ding et al., 2017; Watanabe et al., 2006). Regardless, it is even expected that within a decade or two, global warming will be able to cause 2012 levels of runoff with little or no assistance from the NAO (Bevis et al., 2019). In any case, climate models such as RACMO do not reproduce the turbulent fluxes well during these circumstances (Noël et al., 2015), thus extreme melt events also cannot be modelled accurately, nor can they be reproduced by calculations from weather stations (Fausto et al., 2016; van den Broeke et al., 2017). As in the future these extreme events are expected to occur more frequently (Oltmanns et al., 2019), it is of great importance that this shortcoming is solved. A more realistic 2D field of surface aerodynamic roughness is expected to improve the simulation of turbulent energy fluxes, since a uniform and constant value is presently used in spatially distributed energy balance models (Arnold et al., 2006), while field studies have highlighted the variability of z_0 over ice surfaces in both space and time (Bintanja and van den Broeke, 1995, 1994; Brock et al., 2006; Smeets et al., 1999).

1.2 Aim and research questions

Therefore, the overall aim for this study is to assess different methods to quantify aerodynamic roughness length from topographic roughness based on RPAS data and to quantify its impact on turbulent energy fluxes on the Greenland ice sheet.

To do so, several specific sub-objectives need to be achieved:

1. Assess if RPAS-derived DEMs can be used to quantify topographic roughness
2. Compare different empirical and microtopographic methods to derive aerodynamic roughness
3. Investigate the impact of spatial scale on the aerodynamic roughness estimates
4. Evaluate the impact of the different methods and scale on the magnitude of the turbulent fluxes
5. Assess if the RPAS estimates are comparable to other large-scale datasets

2. Data and methods

2.1 Study site

The studied areas are located in Western Greenland near or on the K-transect (Figure 4). The K-transect is a west-east transect perpendicular to the edge of the GrIS ranging from the low ablation area to above the equilibrium line, along which IMAU and the Free University of Amsterdam started meteorological experiments in 1993 (Oerlemans and Vugts, 1993). The transect is still maintained at this date by the IMAU (Kuipers Munneke et al., 2018). One of these AWS is covered in this study, namely site S5. An overview of the extents, date of capture and which RPAS was used for which area is given in Table 1. The study areas are of different size to showcase the performance of the developed methods for areas of different size.
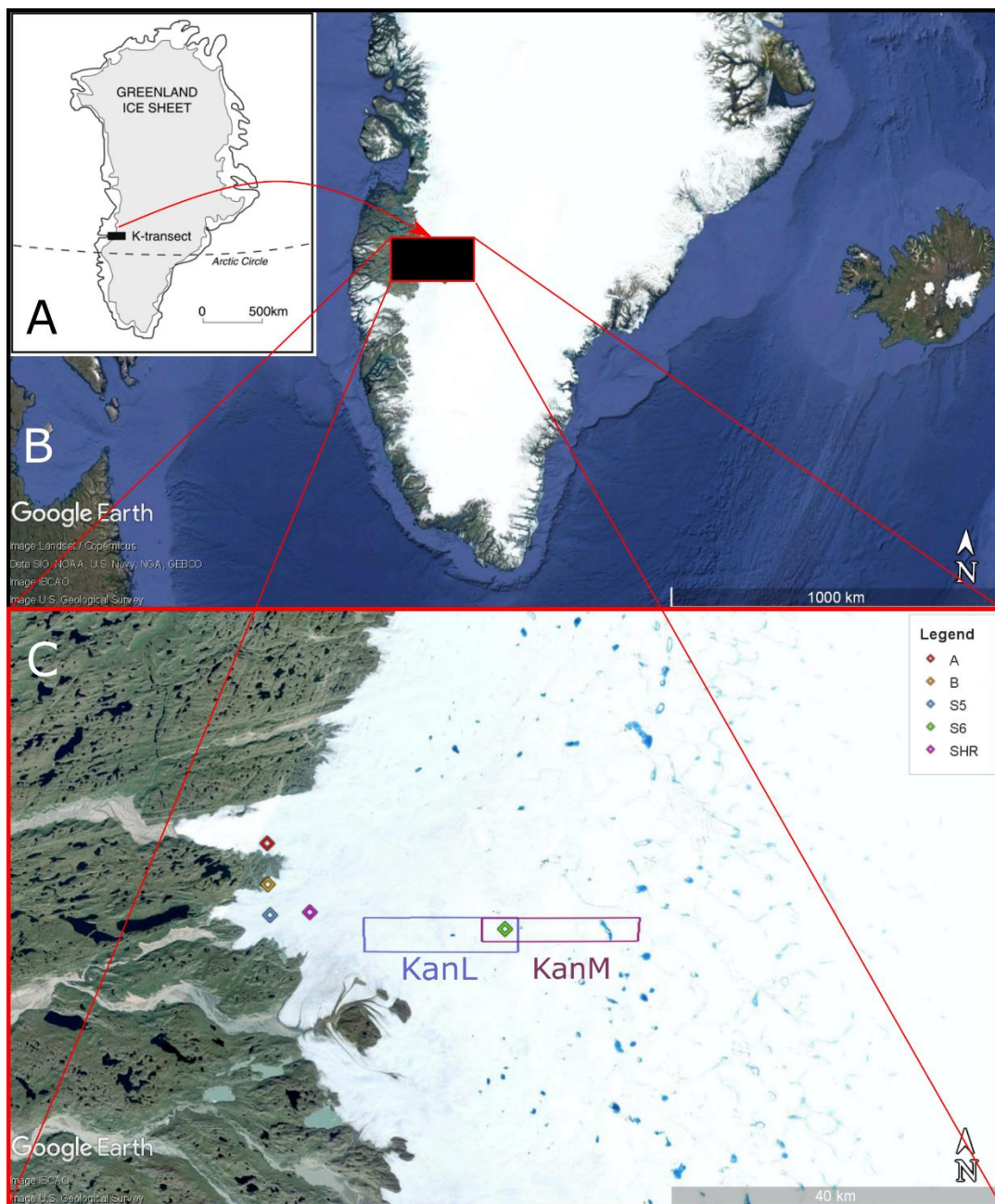
Figure 4. Schematic overview of the location of the K-transect on the GrIS (A) (Smeets and van den Broeke, 2008)*, satellite overview of the location of the K-transect (B), and the locations described in this study (C).*

Table 1. Description of RPAS Images. The Asterix (*) in the column 'Date of Capture' denotes the inclusion of this dataset in the results of this research. The other datasets were processed to DEMs but not included in this research.

Date of capture	Resolution	File-name	Site	Xmin	Xmax	Ymin	Ymax	RPAS
				CRS: WGS84 UTM zone 22N				
08-08-2014*	0.60m	KanL	KanL	552151	570838	7437895	7442562	Skywalker X8
08-08-2014*	0.60m	KanM	KanM	566485	585429	7439502	7442870	Skywalker X8
01-09-2019*	0.30m	F1	A	539346	540750	7450007	7451521	eBee
03-09-20	0.30m	F2	B	539485	540943	7444355	7447208	eBee

19								
04-09-2019	0.10m	S6	S6	569203	569255	7441065	7441119	Mavic Pro
05-09-2019	0.15m	SHR	SHR	545390	545549	7442342	7442715	Mavic Pro
06-09-2019*	0.025m	S5	S5	540434	540811	7441831	7442285	Mavic Pro

2.2 RPAS

The RPAS used for the site A is the eBee developed by senseFly (www.sensefly.com/drone/ebee-mapping-drone/). The eBee airframe is a fixed-wing drone. It has a wingspan of 96 cm and weighs an approximately 0.69 kg including battery and supplied camera. It is wind-resistant to wind speeds up to 45 km h^{-1}, while under benign conditions its cruise speed is up to 90 km h^{-1}. Its maximum flight time of 50 minutes allows for a maximum range of 33 km.

The RPAS used for the site S5 is the Mavic Pro by DJI (www.dji.com/mavic). The Mavic Pro is a quadcopter drone with a diagonal size of 33.5 cm excluding the propellers, weighing an approximate 0.74 kg including camera. Its flight time under normal conditions (with 15% remaining battery) is around 21 minutes. It has a range of 13 km under perfect conditions (e.g. no wind, full battery, constant cruise speed of 25 km h^{-1}).

For information on the RPAS used for the KanL and KanM datasets, the reader is referred to Ryan (Ryan et al., 2018, 2015).

2.3 Cameras

The camera equipped on the eBee airframe was an 18.2 megapixel Sony DSC-WX220. The sensor type of this camera is a 1/2.3" type Exmor CMOS sensor. Its focal length is 4.45mm. The widest possible coverage of this camera gives an angle of view of 82°.

The camera equipped on the Mavic airframe was the standard equipped 12.35-megapixel camera DJI FC220. The sensor type of this camera is a 1/2.3" type CMOS sensor. Its focal length is 4.73 mm. The widest possible coverage of this camera gives an angle of view of 78.8°.

For information on the camera used for the KanL and KanM dataset, the reader is referred to Ryan (Ryan et al., 2018, 2015).

2.4 DEM generation

Agisoft Photoscan software version 1.5.5 build 9097 (www.agisoft.com) is used to create digital elevation models from the RPAS images. Agisoft Photoscan makes use of an image-based surface restitution method which relies on automated, image-to image registration method called Structure from Motion (SfM) (Fonstad et al., 2013; Snavely, 2011). SfM is a form of photogrammetry, which makes use of image matching algorithms that can process images acquired from multiple viewpoints to reproduce the three-dimensional geometry of a surface. It does so by recognizing physical features in multiple images regardless of image scale, and matching these features, which is a simplification to some degree. The image matching algorithms in the SfM workflow of Agisoft Photoscan allow for a high level of automation, and produces excellent results from aerial imagery in a minimum amount of time with almost no effort needed, also enabling non-specialists to produce 3D models from aerial images (Verhoeven, 2011). The DEM of study site S5 (section 2.1) was for instance processed within three hours. For a comprehensive description of the general SfM workflow the reader is directed to Westoby's overview (Westoby et al., 2012). For the workflow related to Agisoft specifically the reader is directed to Immerzeel et al., (2014) or Ryan et al., (2015).

The following parameters are used in the Agisoft workflow. First, the photos were aligned using the "Align photos" function under Workflow. This was performed using the highest accuracy, a key point limit of 120,000, and a tie point limit of 4,000. Hereafter, the cameras were optimized using all optimization parameters of "Optimize cameras" under Tools. Then, the 5% of the points which were deviating most from other points were deleted using the "Gradual selection" under Model, after which the cameras were optimized again. These two steps of optimizing cameras and removing outlier points was repeated 5 times in total. After these steps, the dense cloud was constructed at highest quality using a mild filtering mode in the function "Build Dense Cloud" under Workflow. Lastly, the DEM was extracted from this dense cloud using "Build DEM" under Workflow, enabling interpolation. No GCPs were included in the process of creating the DEMs. This possibly reduces the accuracy of the created DEMs as systematic errors are often observed for DEMs that have limited reference points (James and Robson, 2014).

This DEM is then used to estimate z_0 via a combination of methods that will be explained in section 2.5-2.7, for the purpose of capturing the variability of z_0 across the study area. For comparison, data of the AWS from IMAU will be used. This data is extracted from aerodynamic inversion. A similar approach was previously used by Miles et al., on which this study has built upon (Miles et al., 2017).

2.5 Algorithms

2.5.1 Lettau and Munro

The zero-up crossing method of Lettau (Lettau, 1969) is the basis on which several mechanistic methods to estimate z_0 have been developed. In this method, a linear set of height measurement is

detrended and broken into sections crossing the mean value in an upward direction. The rationale behind this method is that each section crossing the mean value in an upward direction exemplifies an obstacle to wind. Of each obstacle, its length and height are measured, jointly forming a population of obstacles. Then, the method estimates the resistance of flow based on the properties of this population, as is seen in equation (1). This equation uses the average obstacle size h^*, the silhouette area of the average obstacle s (cm^2) and the specific area measured in the horizontal plane (also called the unit ground area) S (cm^2). s and S are defined by equations (2) and (3) following Lettau's nomenclature, where X is the length of the transect and f is the roughness element frequency (number of continuous groups of positive height deviations above the mean elevation).

$$z_0 = 0.5 h^* \frac{s}{S} \tag{1}$$

$$s = \frac{h^* X}{2f} \tag{2}$$

$$S = \left(\frac{X}{f}\right)^2 \tag{3}$$

$$h^* = 2\sigma_z \tag{4}$$

$$z_0 = \frac{\sigma_z^2 f}{X} \tag{5}$$

The Lettau equation for z_0 has been simplified slightly by Munro (Munro, 1989), by taking twice the standard deviation of the elevations, where mean elevation is set equal to zero, for the value of h^* (Munro, 1989). This substitution (4) reduces equations (1-3) to equation (5). The method of Munro has been extensively used in glaciology (e.g. Brock et al., 2006; Miles et al., 2017), since the characterization made by Munro is especially advantageous for glacial surfaces (Munro, 1989). The Munro algorithm was specifically intended to emulate the Lettau results. Ideally applying the two algorithms would yield equal results. However, we also make use of an ensemble of the two algorithms as to account for potential under- or overestimations in either of the algorithms which have been found in some studies. For example, Rounce et al., (2015) found that the Munro method underestimates z_0 in some cases. Some studies (e.g. Smeets et al., 1999) argue that this is due to the fact that the original formula by Lettau was developed for blocks in a wind tunnel, which may not be representable objects with regard to the silhouette area. Furthermore, the Lettau equation lacks the clear definition of what constitutes an obstacle (Rounce et al., 2015). The ensemble is created by calculating the mean of the base 10 logarithms of the output of Lettau and Munro, after which this value is transformed back to non-log values (equation (6)).

$$Ensemble = 10^{\frac{10\log(Lettau) + 10\log(Munro)}{2}} \tag{6}$$

2.5.2 Nield

Nield et al., (2013) developed a range of empirical relationships between z_0 and various surface characteristics, by combining wind tower measurements with terrestrial laser scanning. These empirical relationships were established for small (144m^2), high-resolution plots (0.01m) located on the Makgadikgadi Salt Pan complex in central Botswana (20.5754°S, 25.959°E) (Nield et al., 2013). In this study, only a selection of single-parameter models were considered that have a coefficient of correlation $R^2 > 0.7$. In these empirical relationships, the following SdElev, equation (7)), the standard deviation of obstacle height h_σ (Nield SdObs, equation (8)), mean obstacle height h_{mean} (Nield Mean, equation (9)), and maximum obstacle height encountered for the profile h_{max} (Nield Max, equation (10)).

$$\ln(z_0) = 0.65 + 1.37 \ln(\sigma_z) \tag{7}$$

$$\ln(z_0) = 0.28 + 1.33 \ln(h_\sigma) \tag{8}$$

$$\ln(z_0) = -0.29 + 1.33 \ln(h_{mean}) \tag{9}$$

$$\ln(z_0) = -2.02 + 1.5 \ln(h_{max}) \tag{10}$$

2.6 Detrending methods

2.6.1 Linear detrending

The Lettau and Munro algorithms make use of simple linear detrending regardless of transect length. This is due to the explicit inclusion of transect length X in the Lettau and Munro algorithms, which accounts for the scale dependency. Linear detrending makes use of the best straight-line fit, which is then extracted from the elevation data. An example of a linear model is shown in Figure 5A.

2.6.2 Spline detrending

In contrary to the Lettau and Munro equations, the Nield equations do not contain a length term, and solely rely on the surface characteristics that were used for the established relationships. Furthermore, the established empirical relationships were established form small (144m^2), high-resolution (0.01m) plots located in a salt pan complex which are (relatively) flat morphological features. The resulting plots therefore contain almost no overall topographic trends, which makes detrending redundant for these surfaces. However, the plots that are considered in this study do contain large-scale topographic trends. For the empirical relationships to hold, it is necessary that the plots are comparable. As the plots are not comparable when there is a large-scale topographic trend present, this trend should be removed from the plots prior to further processing.

As is visible in Figure 5, linear detrending does not (fully) remove the large scale topographic trend since the original elevation trend is still visible in the residuals. Therefore, a more powerful detrending technique had to be applied to remove the trend. This paper examined the possibility of spline detrending. A recent comprehensive study on spline functions can be found in Wüst et al., (2017). One key parameter in the spline functions, is the degrees of freedom (DOF) parameter. The DOF is in related to the number of spline sampling points or knots, which divides the area for which the spline is applied into subintervals. For each subinterval, a third-order polynomial is defined, and this induces that more subintervals lead to a better fit. Similarly, lower DOF lead to more constrained splines, higher DOF lead to more flexible splines as more subintervals are present. Figure 5A shows the resulting spline using different DOF on a transect of 200m in length, and Figure 5B shows the residuals in comparison to the residuals from the linear model, while Figure 5C shows solely the residuals from the spline functions. These residuals comprise the data that is used as input for the empirical relationships of Nield. From the figure it can be concluded that the DOF is of great influence on the resulting residuals, and therefore on the roughness estimate by the Nield functions. After examining the influence of DOF on multiple plots and study areas, it was decided that a fixed DOF of 6 was used for the Fixed Grid method (section 2.7.2) to simplify matters, while three different DOF (6, 12, and 18) are tested for the Moving Footprint method that will be in 2.7.1.
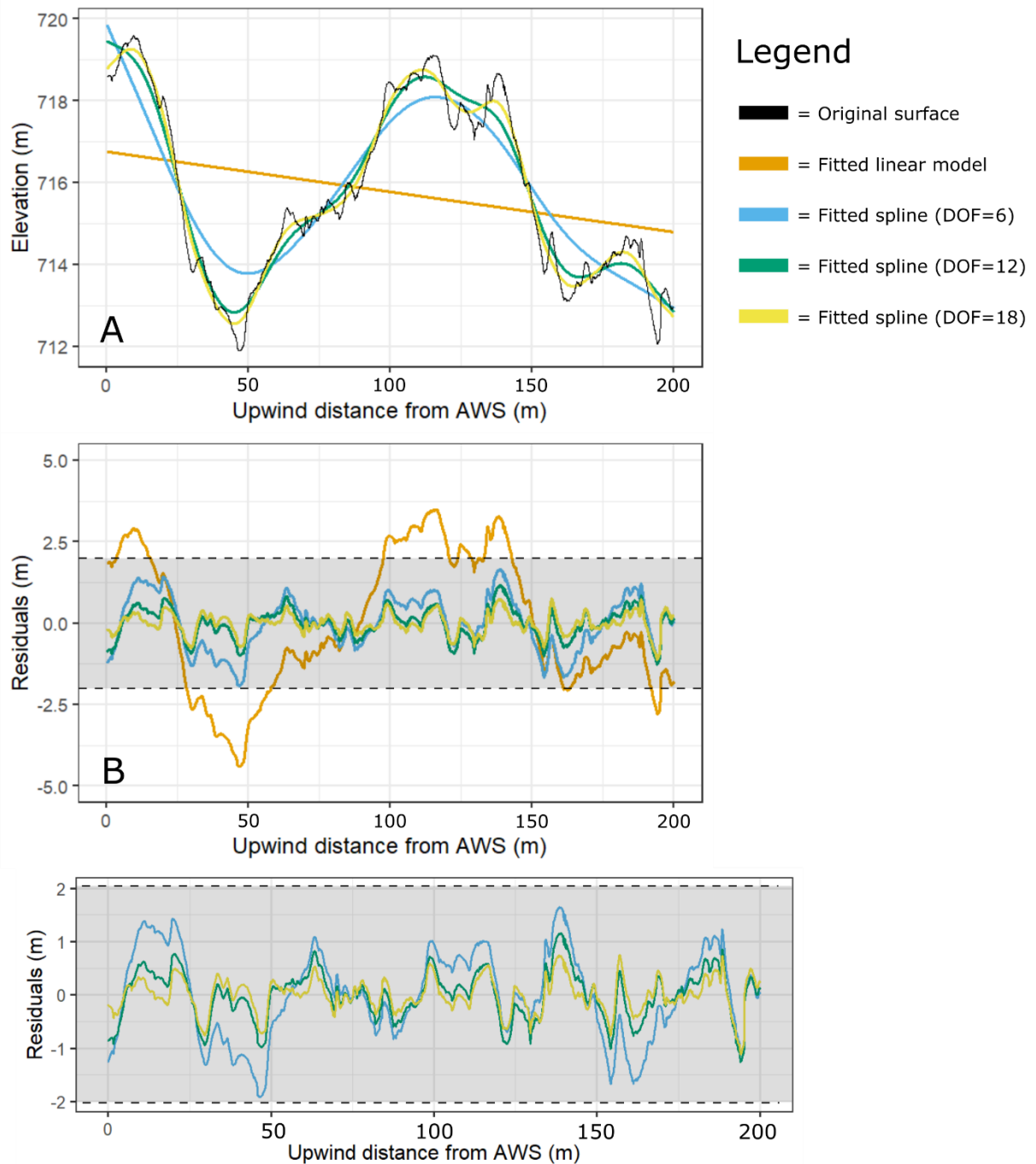
Figure 5. Different detrending methods applied to a random 200m transect of S5. Subpanel A shows the original elevation and the different fitted models. Subpanel B shows the residuals of all fitted models, which are used as input for the Lettau, Munro, and Nield algorithms. Subpanel C shows the residuals for only the fitted spline models and shows that fitted splines with higher DOF result in lower residuals.

2.7 Developed workflow

The study areas were subjected to two different methods that were developed in this study. The first method is called the Moving Footprint (MF) method. This method aims to estimate roughness for a single location by simulating wind over obstacles from certain directions, for example the main wind direction. In short, it does so by considering transects within a rotating footprint to said location, which are then further processed using the Lettau, Munro, and Nield algorithms.

16

The second method is called the Fixed Grid (FG) method. This method aims to estimate roughness for a complete study area with low computational effort. In short, it does so by constructing a grid of specified size over the input DEM, after which in each grid cell, transects are drawn, which are then further processed using the Lettau, Munro, and Nield algorithms.

The difference between the two techniques is thus that the MF method results in roughness values for a single location as a function of direction, while the FG method results in distributed roughness that does not take direction into account. This is a disadvantage as some surfaces of the GrIS are formed in certain directions (Smith et al., 2006), which may not be captured by the FG.

2.7.1 Moving Footprint

The approach for the Moving Footprint (MF) method is as follows.

First, a single location or point around which the MF will rotate should be established. In this case, this will be the AWS location as this will allow us to directly compare the results to the AWS reference data. Then, rectangular shaped footprints of predefined size are created from different directions to the (AWS) location. This is shown in Figure 6A, in which three different footprint sizes (1: 5x40m, 2: 10x100m, 3: 15x200m) are depicted that will rotate around the location of the AWS. The direction can be adjusted to for example correlate to the main wind direction. Within the rectangular shaped footprints, all possible transects in the direction of the AWS i.e. all rows are then constructed. A selection of the possible transects are shown in Figure 6B+C. These transects are then linearly detrended for the Lettau and Munro algorithms, and spline detrended for the Nield algorithms; the reason of this is explained in section 2.6. The detrended transects are then used as input for the algorithms, which results in a z_0 estimate per method, per transect, and per direction. The mean of the z_0 estimate was taken for all transects per method, per direction, which finally results in a directional dependent z_0 estimate per method. The parameters that should be defined prior to applying this method are the size of the footprint, the scope of directions, and the DOF for the spline detrending. A summary of the workflow is given in Figure 9.
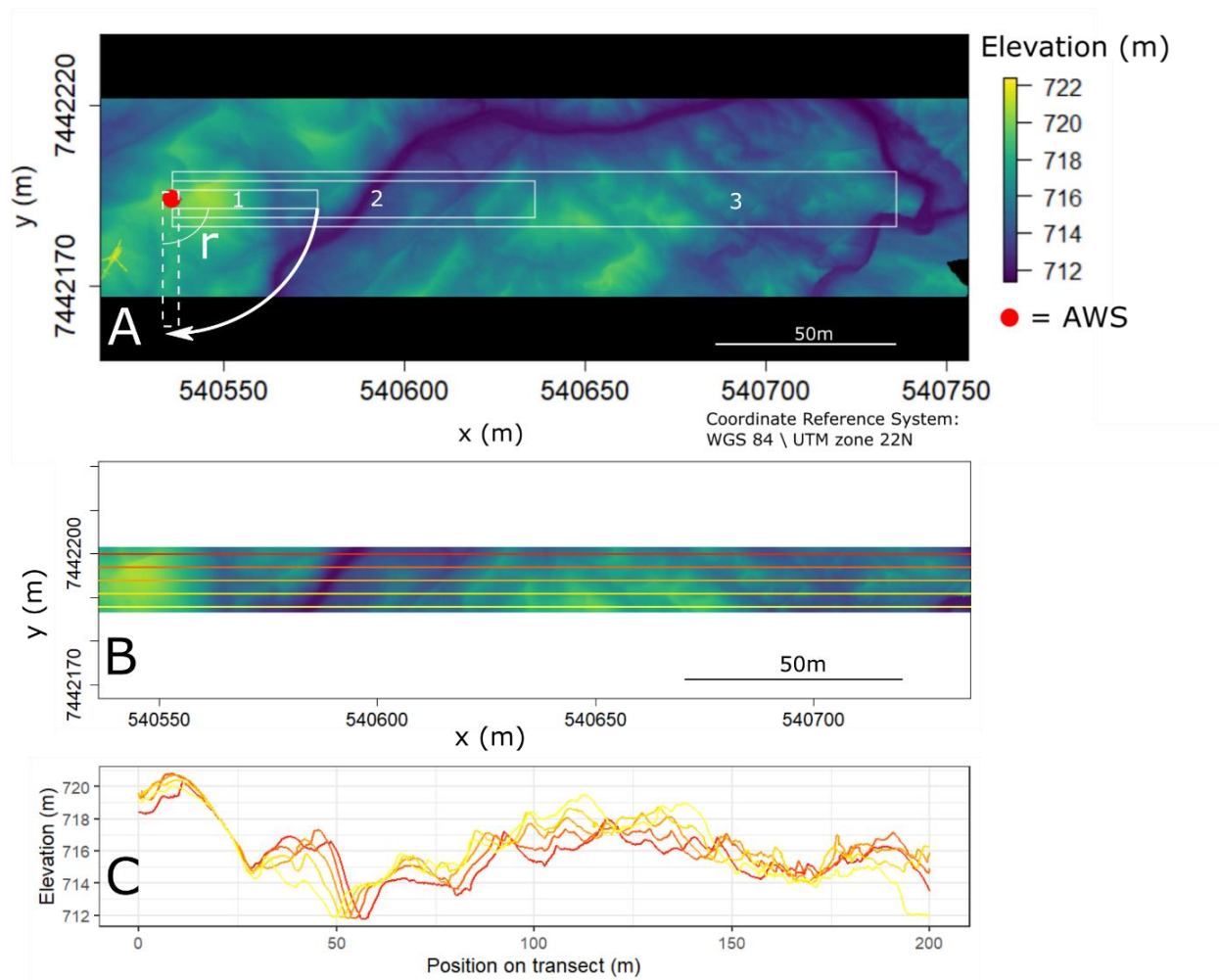
*Figure 6. DEM of a part of S5 showing the outlines of the footprints of different size that were used in the MF method (A), 5x40m (1), 10x100m (2), and 15x200m (3) footprint. The footprint rotates around the AWS location with angle **r**. A single 15x200m footprint is shown (B), including 5 of the possible transects (B+C).*

2.7.2 Fixed Grid

The FG method designed to create distributed z_0 estimates is constructed as follows. First, the input DEM is divided into grid cells of predetermined size, an example of what this division of fixed grids of predetermined size looks like is given in Figure 7A. A multitude of grid sizes are taken as multiple studies have described an effect of grid size on microtopographic estimates (e.g. Kuo et al., 1999; Martin, Valeo, and Tait, 2008; Zhao, Hou, and Wu, 2020). Then, within each individual grid cell, all possible transects in x- and y-direction (Figure 7C+D) containing elevation data were extracted (Figure 7B). All possible transects implies that every row or column of cells is considered. A grid of 10m over a 0.025m resolution DEM yields for example 400 transects in x-direction and 400 transects in y-direction since 10m divided by 0.025m equals 400. These transects were then detrended (again, linear detrending for Lettau and Munro, spline detrending for the Nield equations), after which the algorithms were applied. Hereafter, the mean of all transects per method were taken and assigned to all the cells within the grid, leading to a single roughness value per method per grid block. The resulting distributed roughness value map is thus of coarser resolution than the input DEM. It is also possible in this step to retain the different transect directions, thus leading to two roughness values per method per grid, one for the x-direction (horizontal lines), and one for the y-direction (vertical lines). The overview of the workflow is given in Figure 10.
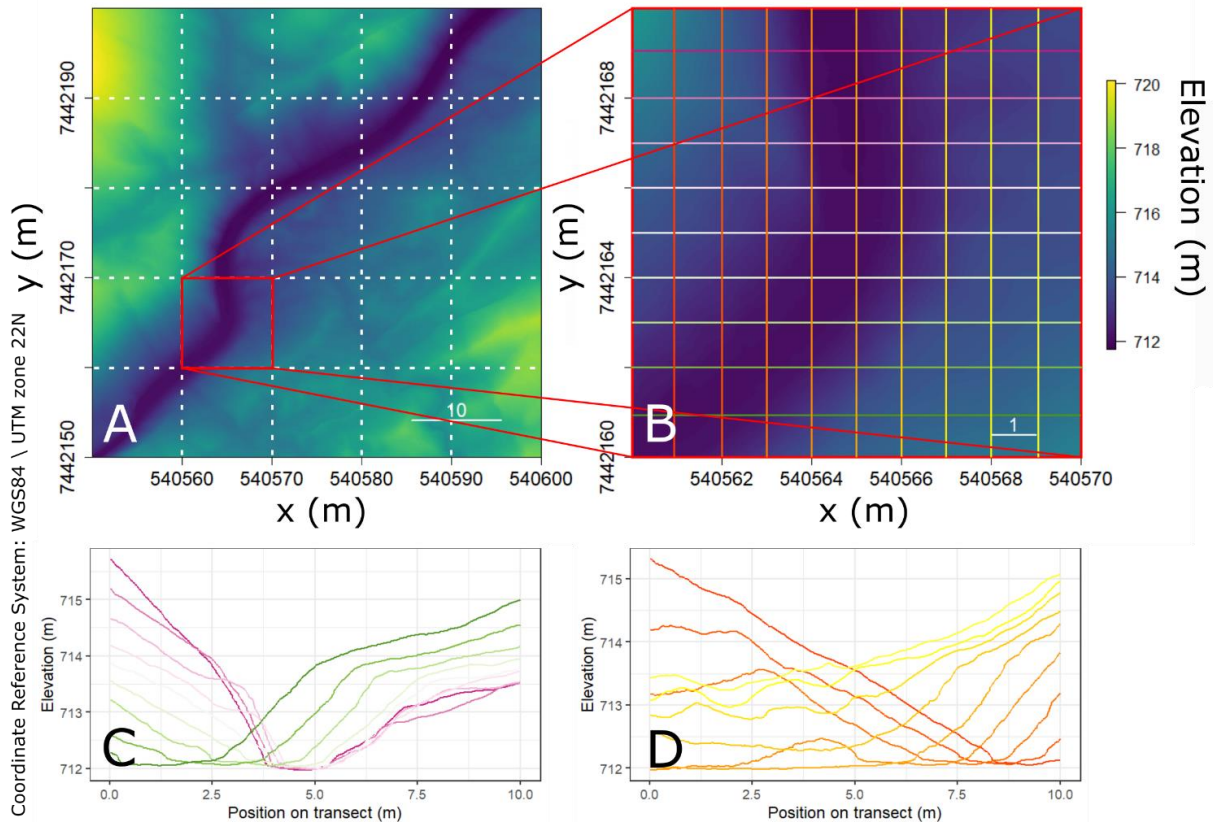
Figure 7. Figure clarifying the Fixed Grid method. A DEM of the study area is segmented in grids of specified size (A), in this case 10x10m grid. Within this grid (B), all possible transects are drawn in x-direction (C), and y-direction (D). Now, only the transects at 1m intervals are shown, while the method itself considers every possible transect i.e. every row or column of cells. Each single resulting transect is then further processed through detrending and subsequent input in the algorithms.

While the nature of the results is inherently different for the FG method and the MF method (distributed results vs location-specific), a simple approximation is used to allow the comparison of results. This approximation is the movement of the Moving Footprint over the distributed results of the FG method, which returns the mean value within the footprint. This allows us to simulate directional influence on the z_0 estimate. An example is given in Figure 8.
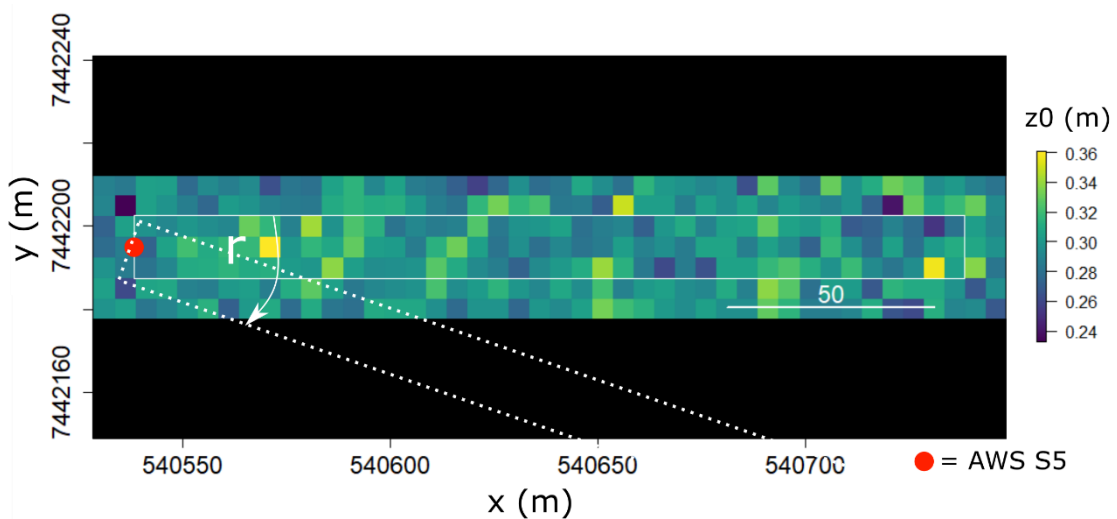

Figure 8. Simplified Moving Footprint which moves over the Fixed Grid distributed result for grid size 5m. It calculates the mean value inside the footprint, therefore, producing z_0 values as a function of angle r.

The Fixed Grid method makes use of an arbitrary fixed grid that is placed over the DEM as is previously explained. The use of an arbitrary grid may potentially cause inaccuracies, as every cell within the fixed grid is assigned the same value. A moving focal instead of a fixed grid could potentially compensate for this error. However, the required computational power is roughly 40000 times greater for the smallest grid size (5m) that was examined in this research, as is explained by the following example. In the current FG method, for each grid of e.g. 5x5m, the algorithms are applied for every possible transect within said grid. The results are then averaged for said grid, and assigned to every cell within the grid, resulting in a single value for the 5x5m grid. The moving focal would create a grid of e.g. 5x5m around each cell, in which the methods are applied for every possible transect, averaged, and then assigned to the single cell. After which, it moves to the next cell. As the resolution of the data is 0.025m, and the example grid size is 5m, it would have to apply the functions 200 (5m/0.025m=200) times extra in x-direction and 200 times extra in y-direction, thus 40000 times extra to cover the same area as the FG approach. Therefore, this method was not a realistic option for the aim of this study, namely producing distributed roughness estimates with low computational effort.

2.7.3 Used parameters

The parameters that were used in this study are summarized in Table 2. As was mentioned in section 1.1.2, the spatial resolution is of importance for the roughness-partition scale. Consequently, different spatial resolutions were considered to examine the scale-dependency of z_0. Other research often also includes the exploration of the impact of spatial resolution on e.g. the modelling of surface mass balances of the GrIS (Franco et al., 2012). Therefore, the DEM of S5 was coarsened to resolutions of multiple scale magnitudes by averaging. Hereafter, the coarsened DEM was processed like the original DEM, and z_0 was calculated for this DEM as well.

Table 2. Parameters used in this research for the two developed methods.

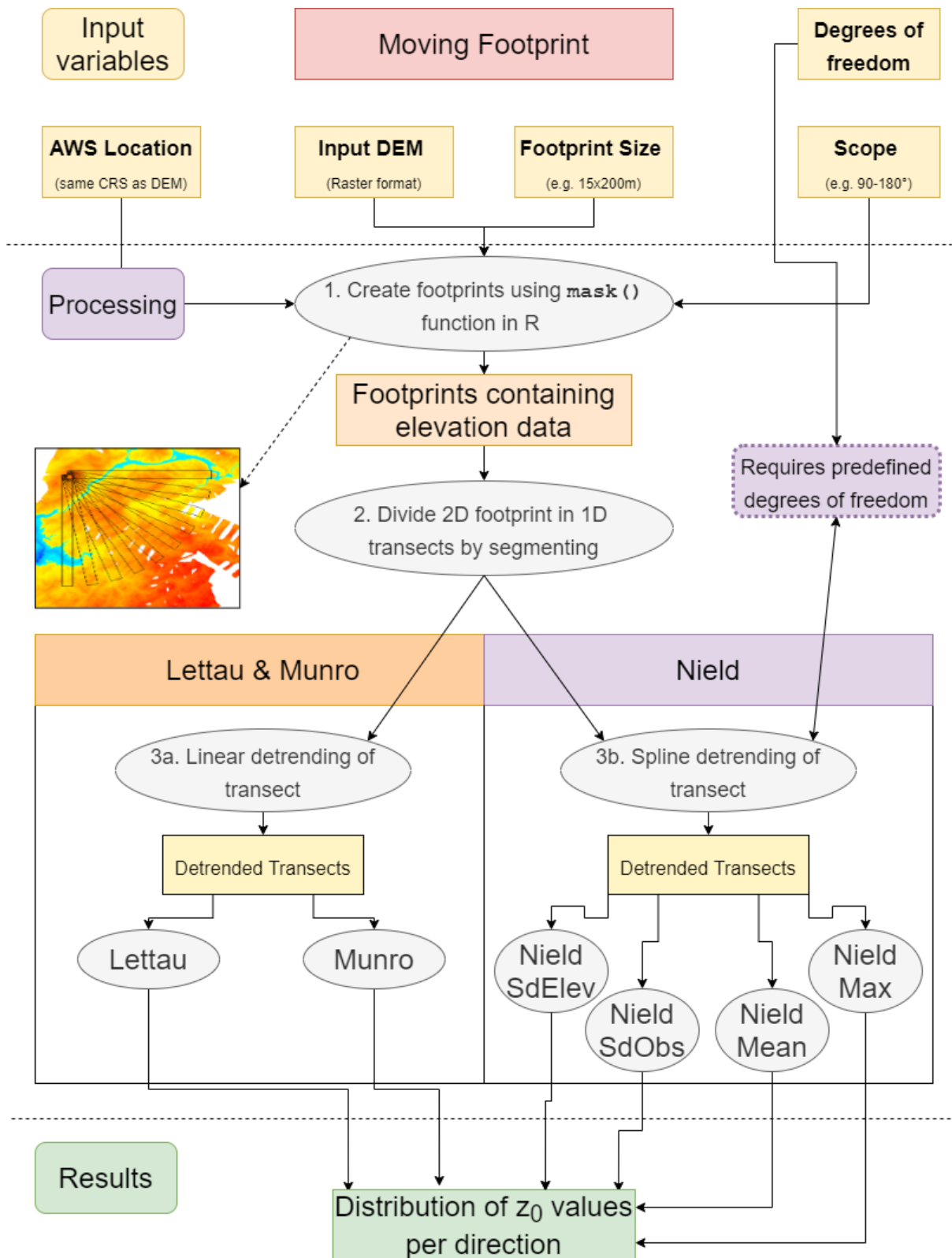| Site	Original Resolution	Moving Footprint			Fixed Grid
		Coarsened Resolutions	Footprint size	Scope of directions	Grid size
S5	0.025m	0.05m, 0.5m, 1.0m, 2.5m, 5.0m	5x40, 10x100, 15x200	90-180°	5m, 10m, 15m, 20m
A	0.30m				30m
KanL	0.60m	Moving footprint not applied to these datasets			90m
KanM	0.60m				90m

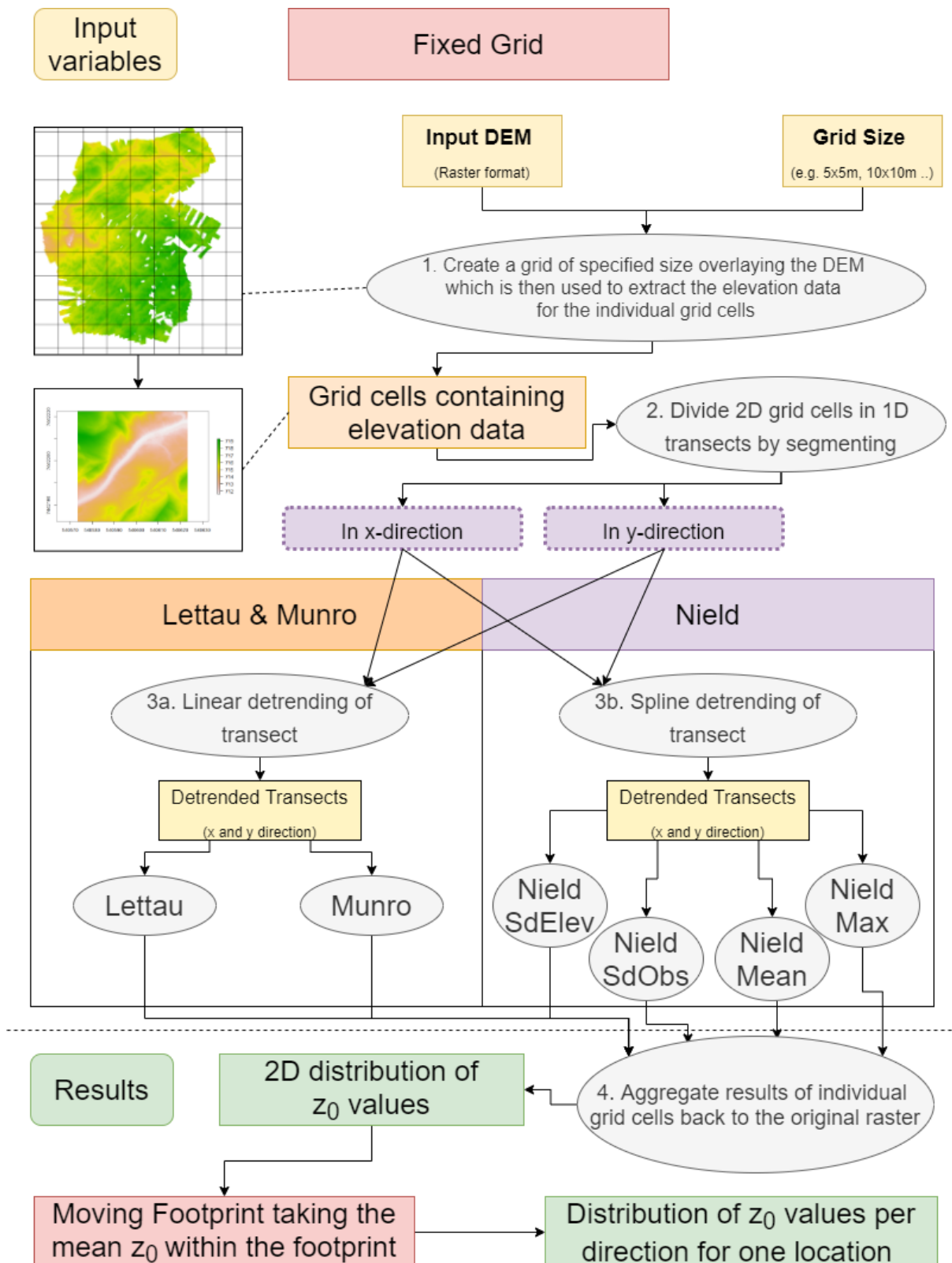*Figure 9. Workflow of the Moving Footprint method*

Figure 10. Workflow of the Fixed Grid method

2.8 Turbulent flux estimation

As the z_0 is used in the calculation of turbulent fluxes, we are interested in what consequences the resulting z_0 values have for these fluxes. Therefore, the turbulent fluxes were estimated using the z_0 values obtained in the previous part of this study. The resulting flux estimate can then be compared to the sensible heat flux that was measured by the eddy-covariance system. It can also be compared to the simulated fluxes using the aerodynamic roughness length derived by applying the profile aerodynamic method based on Monin-Obukhov using the AWS observations. A clear example of how aerodynamic roughness length is derived from AWS observations can be found in Sicart et al., (2014).

Turbulent fluxes were estimated with the commonly used bulk aerodynamic method (Munro, 1989), using data collected by the AWS. The bulk aerodynamic method consists of a set of Equations that solve the Monin-Obukhov length $L*$ (m) with an iterative process. We focus on the sensible heat flux H (W m^{-2}), equation (10).

$$H = \rho_a c_p k^2 \frac{u(T_a - T_s)}{(\ln\left(\frac{z_v}{z_0}\right) - \psi_m(\frac{z_v}{L_*}))(\ln\left(\frac{z_t}{z_{t0}}\right) - \psi_h(\frac{z_t}{L_*}))} \tag{10}$$

Where ρ_a (kg m^{-3}) is the air density, c_p (J K^{-1} kg^{-1}) is the specific heat of dry air at constant pressure, k (0.4) is the von Karman constant, T_a (K) is the air temperature, T_s (K) is the surface temperature, u (m s^{-1}) is the windspeed, z_v z_t z_q (m) are the levels at which windspeed, temperature and humidity levels are measured, z_0 z_{t0} z_{q0} (m) are the roughness lengths for momentum, sensible heat and humidity. Normally the potential temperature difference is used to account for the adiabatic heating of a downwelling air parcel, but for small height differences it is roughly the same to $T_a - T_s$. Typically, the z_{t0} and z_{q0} are one or two orders of magnitude smaller than z_0 (Cullen et al., 2007; Radić et al., 2017; Smeets et al., 1998), but it is known that the ratio depends on the roughness Reynolds number (Andreas and Murphy, 1986; Smeets and van den Broeke, 2008). The modelled sensible heat flux greatly depends on the roughness length of heat, which is calculated by the bulk model of Smeets and van den Broeke (2008).

3. Results

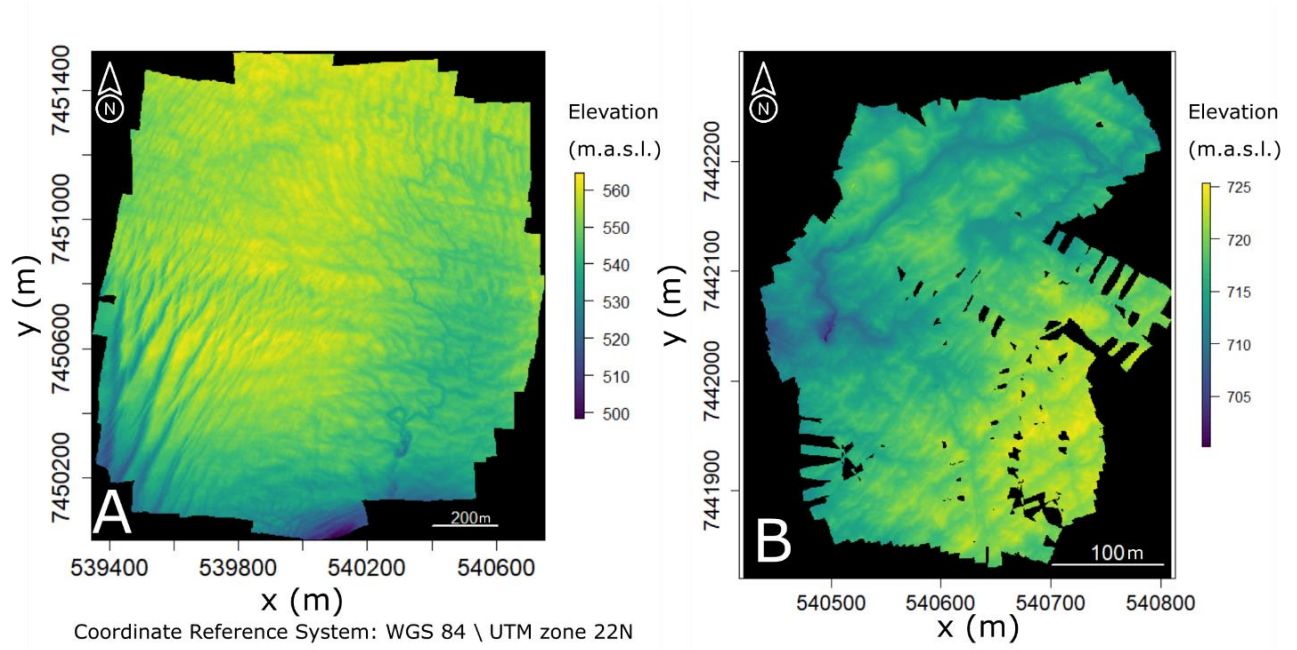## 3.1 Overview of Digital Elevation Models

Figure 11. Digital Elevation Models of site A (A), and S5 (B). The DEMs for the areas A and S5 were produced in this study using Agisoft. The DEMs for KanM and KanL were produced by Jonathan Ryan (Ryan et al., 2018, 2015) of which a subset was taken in this research.

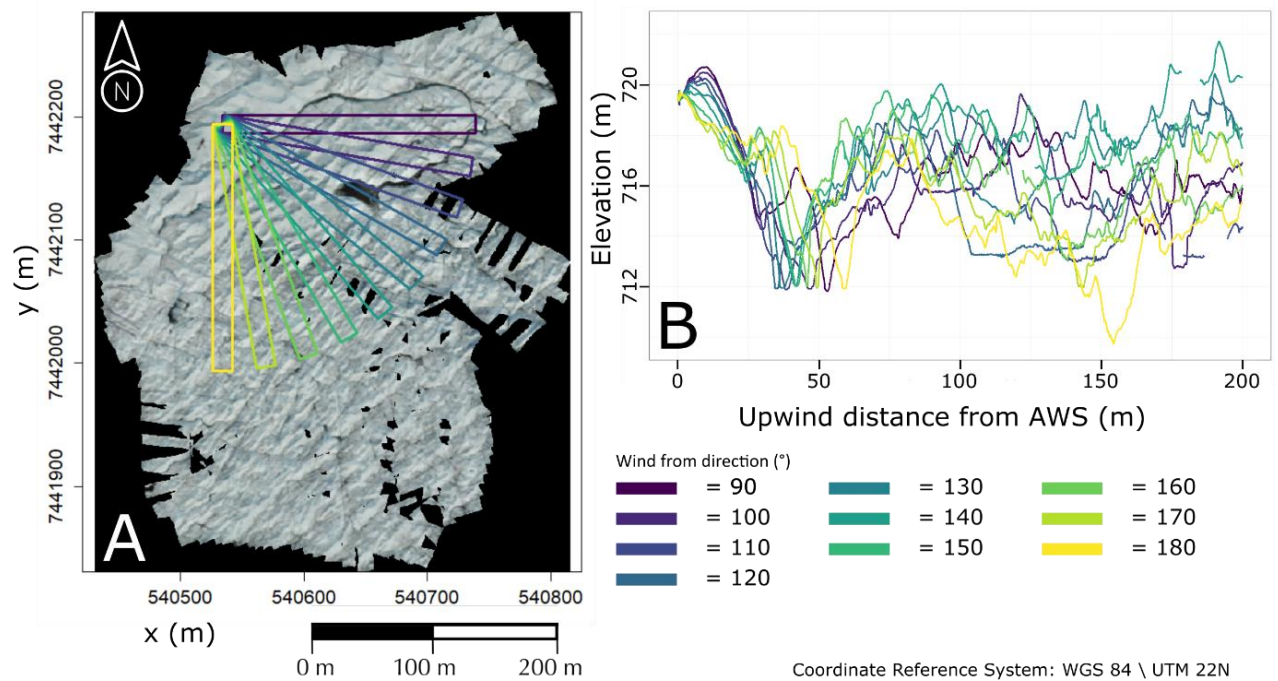## 3.2 Moving footprint estimated roughness

Figure 12. Orthomosaic of S5 including a selection of the outlines of the footprints that were taken when using the moving footprint of 15x200 (A), including the transects (B).

3.2.1 Lettau & Munro

Figure 12A shows a selection of outlines for which the elevation data was considered in the algorithms, and Figure 12B shows the correlating transects, illustrating the variation in elevation. In Figure 13 the resulting estimated values for z_0 are shown on a logarithmic scale per direction for each footprint for the Lettau and Munro algorithms. The resulting estimated values for z_0 differ per footprint size, for both the Lettau as the Munro algorithm. The largest difference in estimated z_0 is visible between the 5x40m (A) and the 10x100m (B) footprint. The 10x100m (B) and 15x200m (C) footprint are more similar. Between the two algorithms, a large difference is also noticed. The estimated z_0 values by Munro are roughly an order of magnitude higher than the estimated z_0 values by Lettau. The values for Lettau are more variable over directions and seem to capture some of the directional dependence that the AWS also captured. Noticeable is also the directional differences per footprint. The 5x40m footprint finds the largest z_0 value around 120°, while the largest z_0 values for the 10x100m footprint and the 15x200m footprint are found around 170° and 155°. The Munro algorithm seems to capture less directional differences within the z_0 estimate. It should be noted that the reference data only provided an estimate of z_0 for the range of directions 97° to 149°.
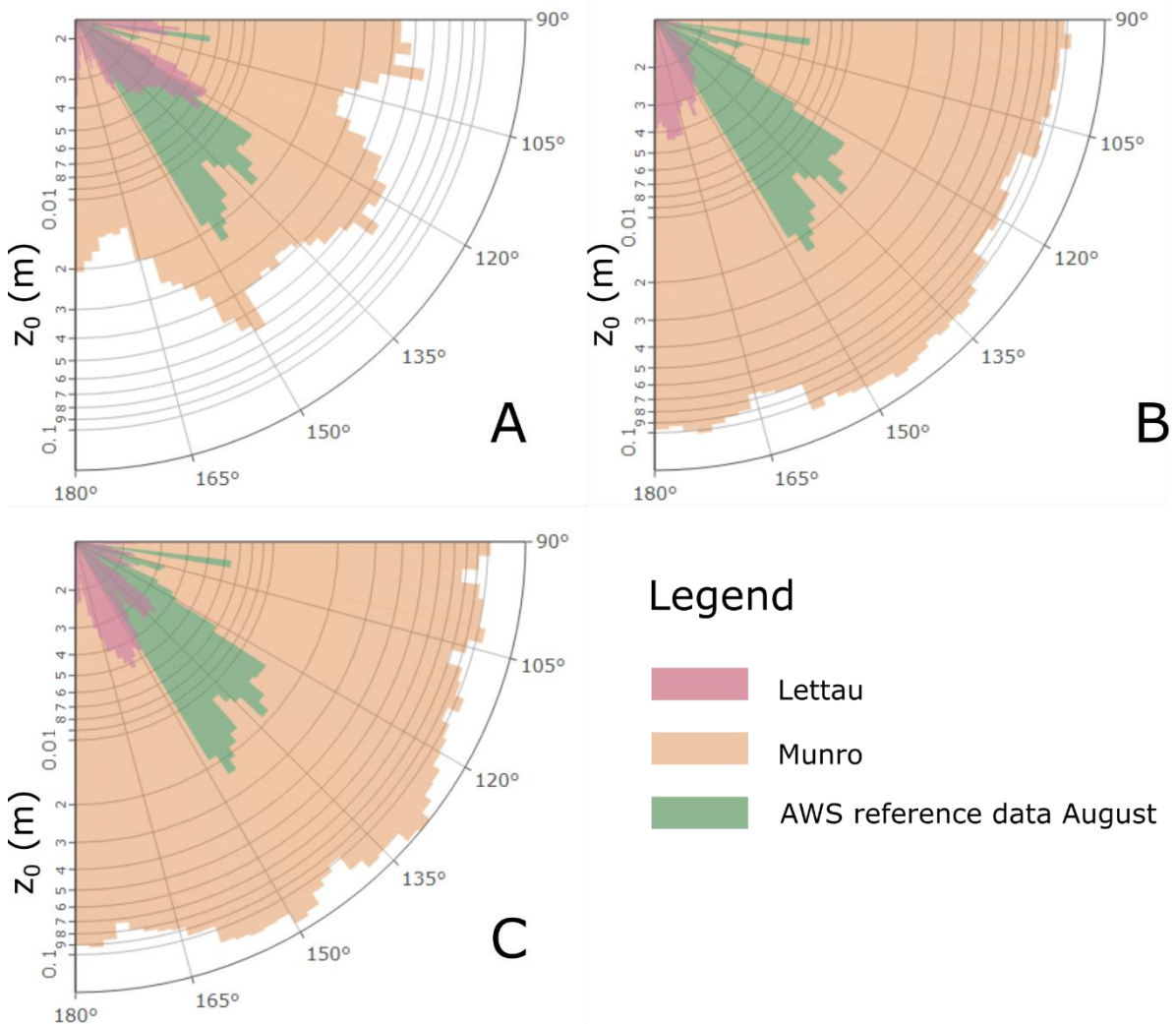

Figure 13. Results for the MF method binned per 2 degrees, from 90-180°, for footprint sizes 5x40 (A), 10x100 (B), and 15x200 (C). The AWS reference data is of August 2019.

25

3.2.2 Lettau-Munro ensemble

In Figure 14 the results are shown per direction for the Moving Footprint for the Lettau and Munro algorithms.

Multiple differences are noticeable in this figure. Firstly, the differences in the magnitude of estimated z_0 between the three footprint sizes are less significant when compared to the differences in magnitude of estimated z_0 between the footprint sizes for Lettau and Munro. Differences in z_0 estimates per direction remain, though the values are roughly in the same order of magnitude. The 15x200m footprint (Figure 14C) seems to capture both value and direction similar to the AWS reference data. Furthermore, the values are in the same order of magnitude as the AWS reference data.
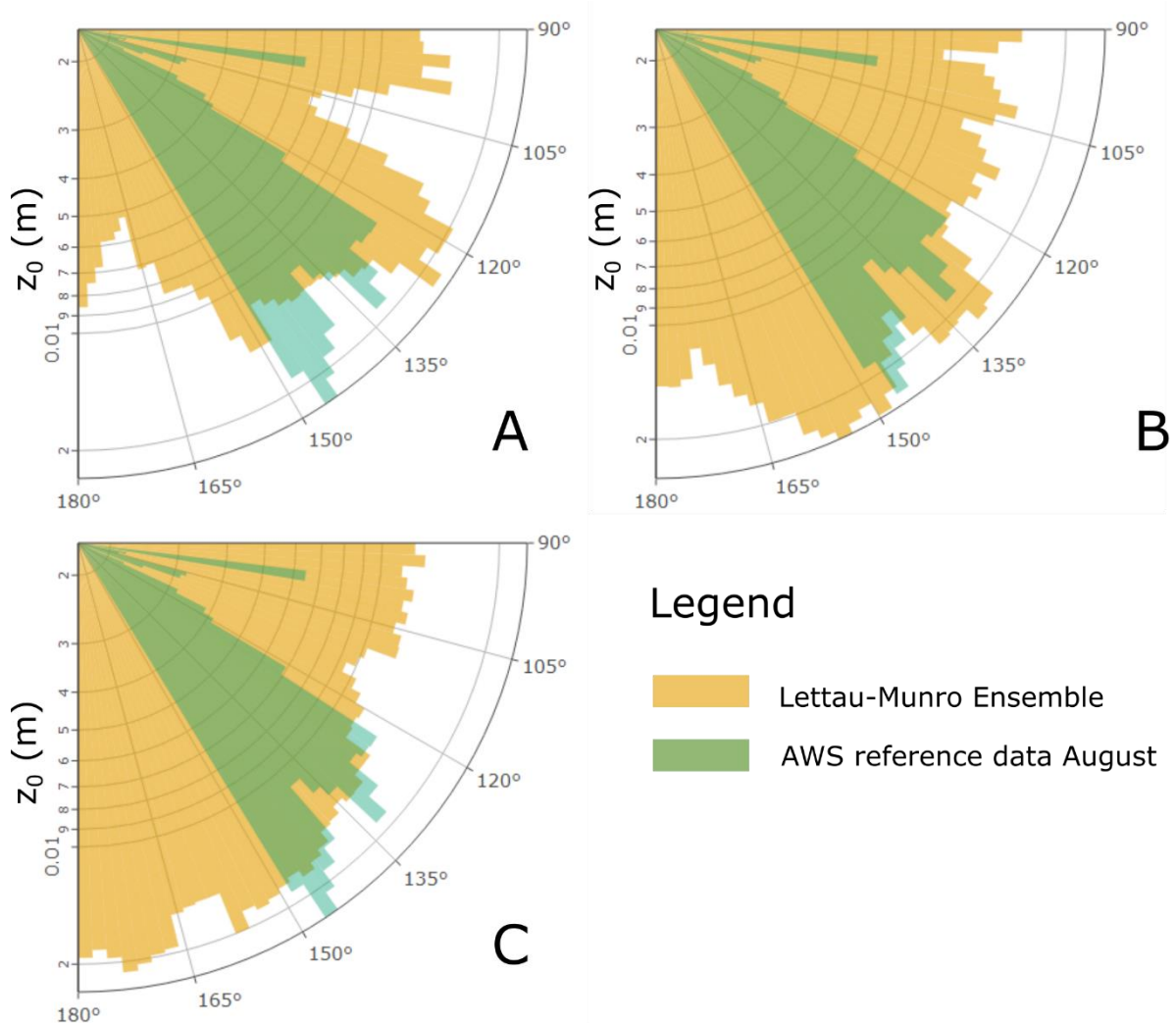

Figure 14. MF results for Lettau-Munro ensembles, binned per 2 degrees, from 90-180°, for footprint sizes 5x40 (A), 10x100 (B), and 15x200 (C). The AWS reference data is of August 2019.

3.2.3 Nield fixed DOF

Figure 15 and Figure 16 summarizes the resulting z_0 estimates in identical to previous polar plots, only now for the Nield functions. It reveals immediately the performance of the different Nield algorithms. Nield SdElev and Nield Max (Figure 15) both show a similar pattern for the 5x40m footprint (A) with high estimated z_0 values in the directions 120-130° and 170-180°, and produce z_0 values in an order of magnitude similar to the AWS albeit slightly higher. For Nield Max and Nield SdElev the observation can be made that an increase in grid size leads to higher roughness estimates. The similarity of patterns of Nield Max and Nield SdElev can be observed throughout all footprints.

Figure 15. Results for the algorithms Nield SdElev & Nield Max applied in the Moving Footprint 5x40m (A), 10x100m (B), and 15x200m (C). The AWS reference data is of August 2019. Large differences in magnitude are observed for the different footprints. Similar directional patterns are also observed for these two Nield functions.
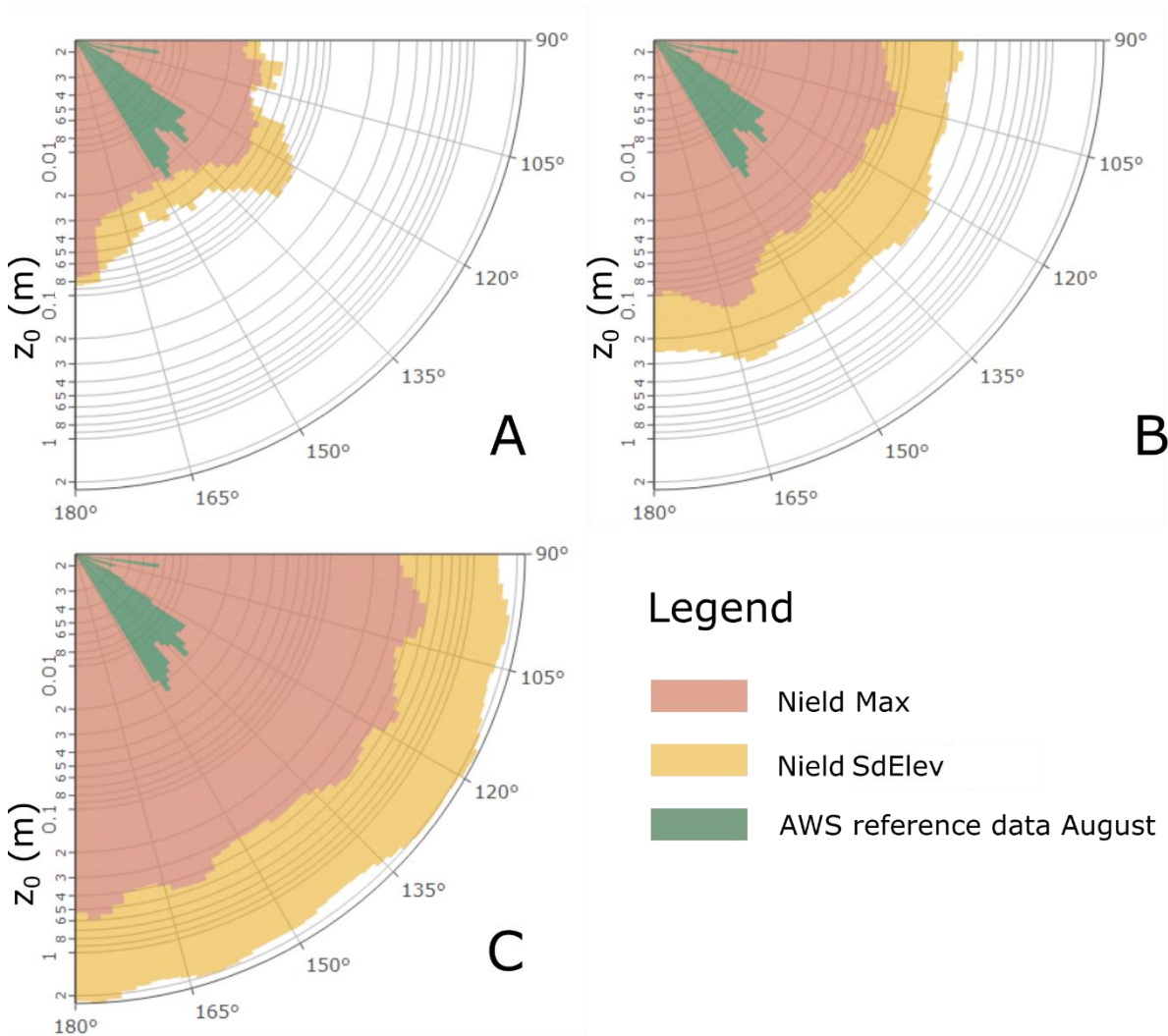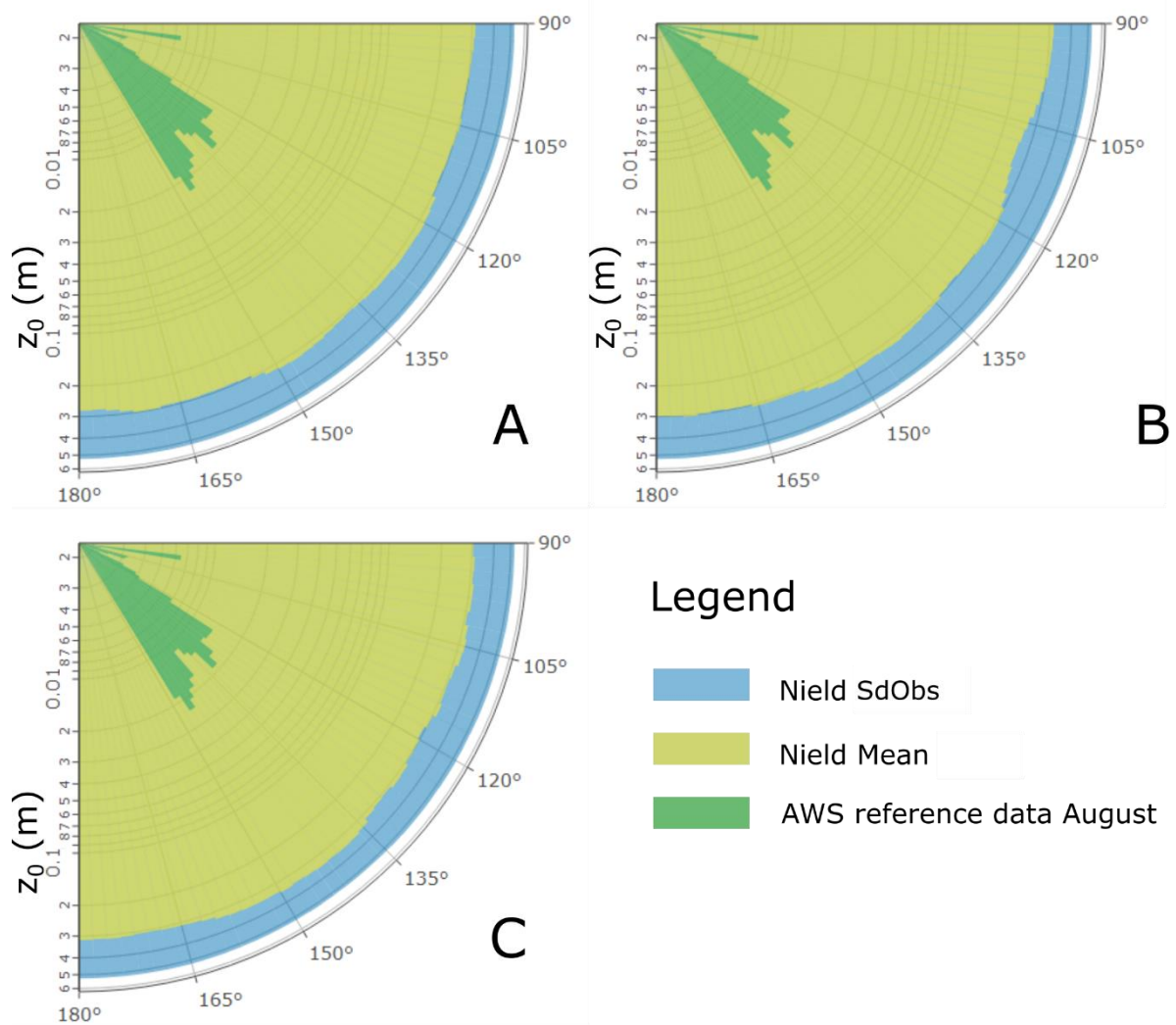
Figure 16. Results for the algorithms Nield SdObs & Nield Mean applied in the Moving Footprint 5x40m (A), 10x100m (B), and 15x200m (C). The AWS reference data is of August 2019. No differences in magnitude are observed for the different footprints. Furthermore, none of these methods seem to capture directional influence, as the variation in estimated values is very little.

The other Nield algorithms, Nield SdObs and Nield Mean (Figure 16), produce estimates for z_0 that are at least an order of magnitude larger compared to the reference data. None of the footprints seem to capture directional differences, as very little variation is observed over the different angles. When comparing the different footprints, it is clearly observed that between the different footprints, little to no differences can be discerned.

3.2.4 Nield variable DOF

For the algorithms Nield SdObs and Nield Mean we established earlier that footprint size had no influence on the resulting z_0 estimate, which induces that they are also insensitive to increasing the DOF. Therefore, only the Nield SdElev and Nield Max were considered in this section, where the influence of the DOF of the spline detrending is examined. By examining Figure 17, multiple observations can be made. First, an increasing DOF results in a lower estimate for z_0. This is understandable, as increasing the DOF, decrease the metrics on which these Nield functions are based, and thus reduce the resulting z_0 estimate. More interestingly, the directional variation does not seem to be affected by the changing DOF.
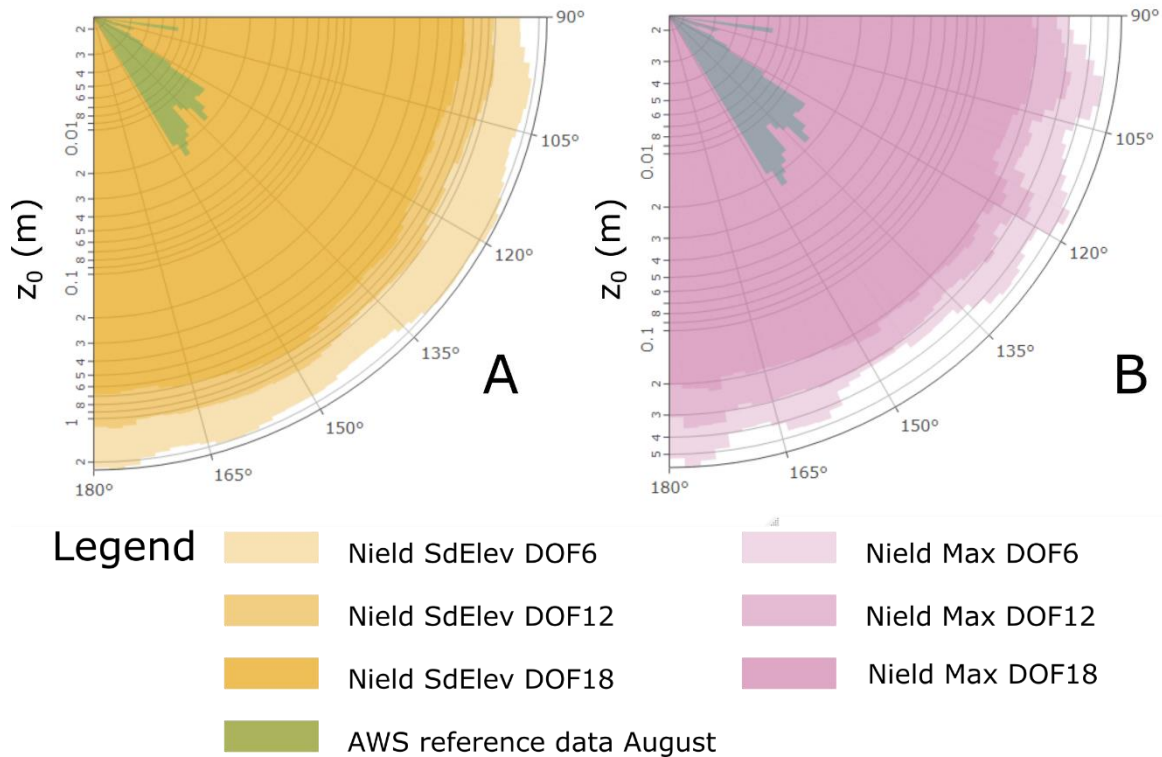
Figure 17. Results for the Nield algorithms Nield SdElev (A) & Nield Max (B) applied in a 15x200m Moving Footprint using multiple DOF for the spline.

3.3 Fixed grid estimated roughness

The distributed results of the FG method are not directly comparable to the AWS reference data as the results are distributed over the study area instead of location-specific results, thus the distributed results are compared by the estimated values for z_0, and their spatial patterns. Selected spatial distributions of z_0 are included in the results. Note that the scales are not equal. This was done purposefully as some results contained very little variation (e.g. Figure 18F) which complicate the illustration of these figures.
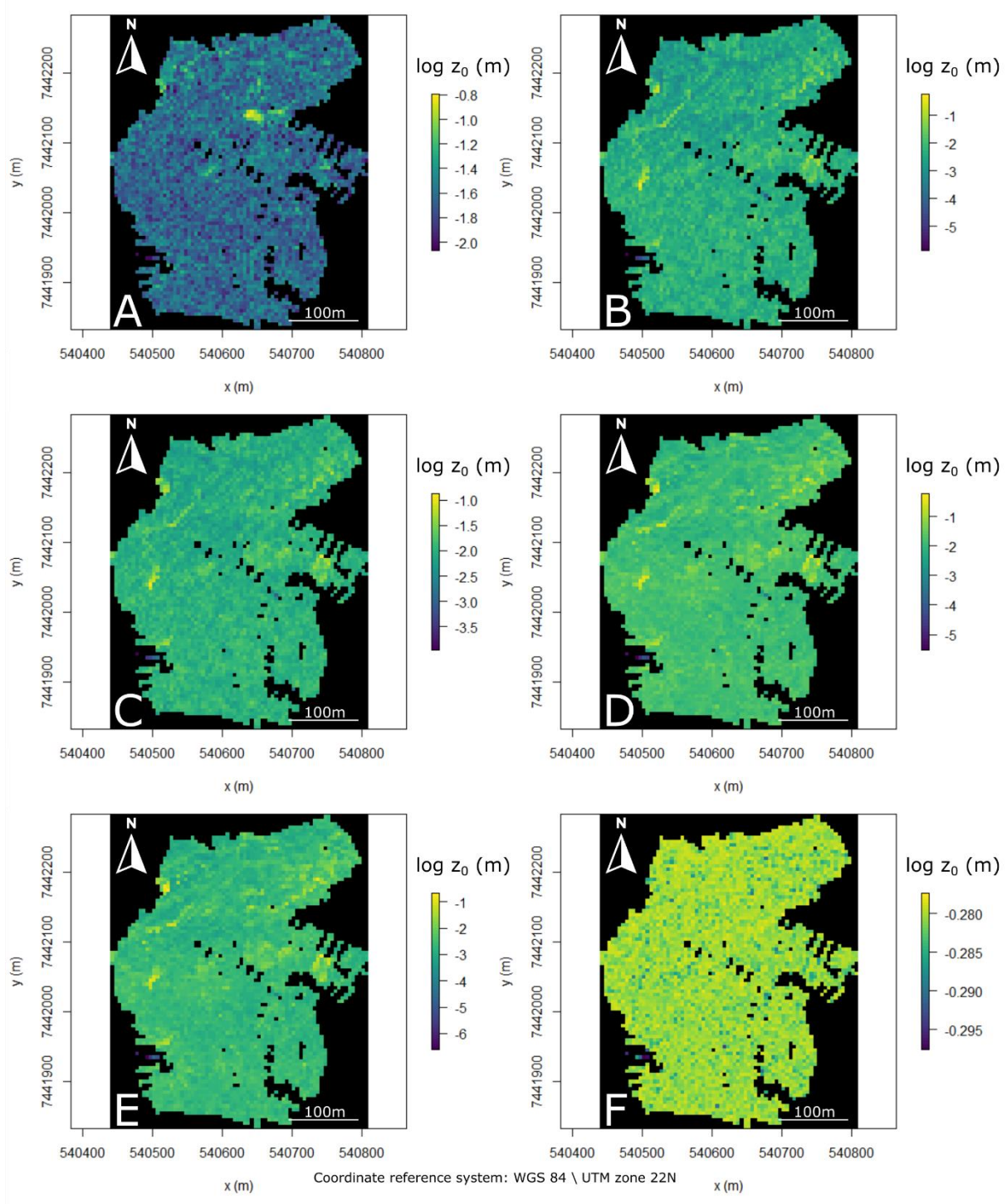
Figure 18. Distributed results for 5m grid size for Lettau (A), Munro (B), Lettau-Munro Ensemble (C), Nield SdElev (D), Nield Max (E), and Nield SdObs (F).

3.3.1 Lettau & Munro

When visually examining the distributed results for the 5m grid size (Figure 18), a noticeable difference between the two algorithms is present. The Lettau algorithm (A) shows an area of high z_0 values around position x=540630, y=7442140, which the Munro algorithm (B) does not show. This correlates to a small meltwater lake, which is visible on the orthomosaic (Figure 12). Meanwhile, in the distributed result of the Munro algorithm, the meltwater river is identifiable, in contrast to the Lettau results.

The variation within the estimated roughness values of the study area is up to two orders of magnitude (e.g. 0.001-0.1m for Munro at 5m grid size). This is a realistic range, as the estimated roughness by the AWS has a similar range of values. The FG method does seem to overestimate the roughness for all grid sizes and algorithms, except Munro 5m, as the values are at most an order of magnitude higher than what is expected when comparing to the reference values.

Figure 19 shows the distribution of values displayed in a violin plot for Lettau, Munro and the Lettau-Munro ensemble. Both the Lettau and Munro algorithms exhibit a sensitivity to grid size. Interestingly, the patterns are the opposite for Lettau and Munro. The Munro algorithm shows a tendency to produce a higher estimate for z_0 as the grid size increases. The Lettau algorithm shows a tendency to produce a lower estimate for z_0 as the grid size increases. More interestingly, the Lettau-Munro Ensemble roughness estimate remains (almost) equal over the grid sizes.
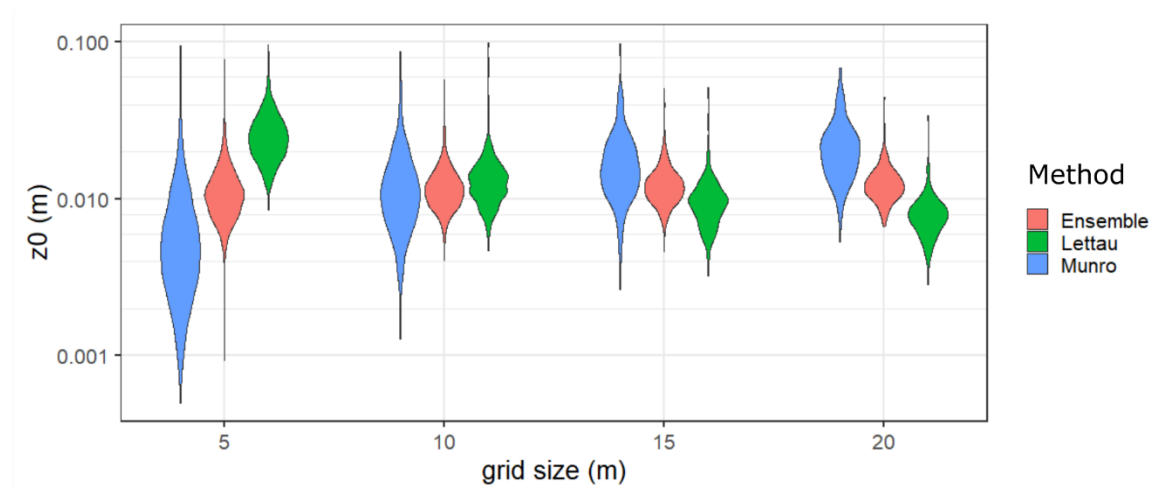
Figure 19. Estimated z_0 values for the Lettau & Munro algorithms and their ensemble displayed in violin plot format. For Lettau, a downward trend is observed with increasing grid size, in contrast to Munro for which an upward trend is observed. The z_0 estimates of the ensemble are not influenced by grid size.

3.3.2 Nield
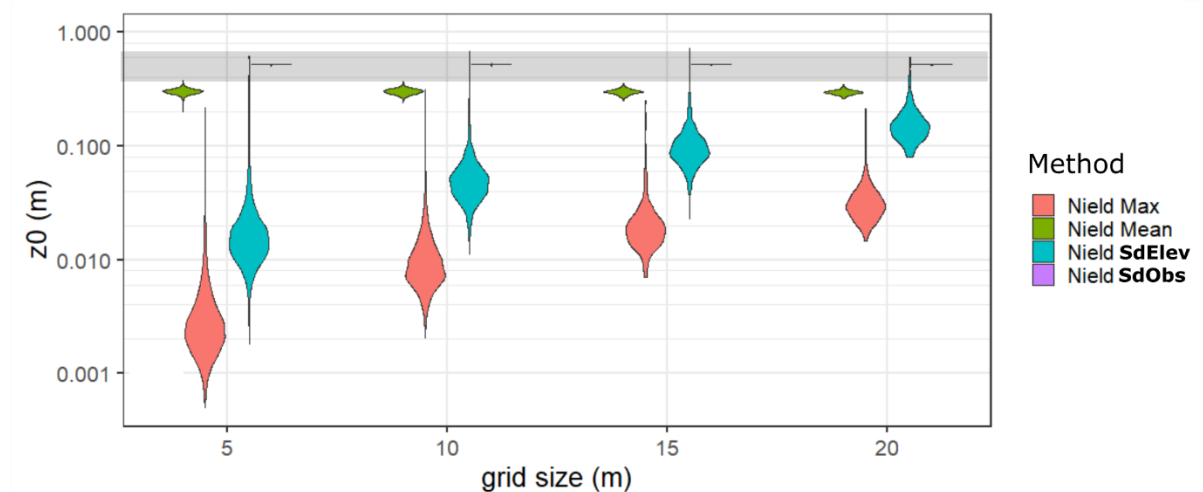
Figure 20. Estimated z_0 values for the Nield algorithms displayed in violin plot format. For Nield SdObs (located inside the grey band) the violin plots are not visible due to the extremely low variation within the z_0 estimate. It can be observed that grid size does not influence the z_0 estimate of Nield SdObs and Nield Mean, as the values remain equal regardless of grid size. For Nield Max and Nield SdElev it is visible that a greater grid size result in higher z_0 estimates.

Figure 20 shows the distribution of values displayed in a violin plot for the different Nield algorithms. From this figure it can be concluded that Nield SdObs and Nield Mean are not affected by the different grid sizes that were taken. This in contrast to Nield SdElev and Nield Max. Nield SdElev and Nield Max both show the tendency to produce higher z_0 estimates as the grid size increases, similarly to the Munro algorithm. Furthermore, the spread within the roughness estimate is much less within Nield SdObs and Nield Mean. For Nield SdObs, the values produced by this algorithm ranged from 0.50-0.52m.

The range of values produced by Nield SdElev and Nield Max span roughly an order of magnitude and contain slightly less variation then the Lettau and Munro algorithms.

3.4 Moving footprint over fixed grid estimated roughness

A way how a meaningful comparison can be made between the FG method and the AWS reference data is to visualize the data as a function of wind direction. The way this was performed was by producing a moving footprint in which the mean for each footprint was taken, in contrast to the MF technique where the algorithms were applied within each footprint.

3.4.1 Lettau & Munro

As was expected by examining Figure 19, the estimated roughness values for Lettau are substantially higher than the estimated roughness values for Munro. Also, Figure 21A strengthens the believe that Munro captures more spatial variability over direction than the Lettau algorithm, as the estimated roughness values for Munro vary more with direction. At 118° the estimated z_0 is roughly 0.005m, while at 94° this is roughly 0.010m, an absolute difference of 0.005m, and a relative difference of factor 2. For Lettau the resulting values are less variant in direction, resulting in values in the range 0.022-0.032m. In absolute terms, this difference between lowest and highest value is high (0.01m), while relatively, this difference is lower than within Munro (factor 2 versus factor 1.46). Furthermore, two peaks of Munro seem to coincide with peaks in the AWS data, namely the peak at around 130° and 145°, though the estimated values for z_0 for Munro are significantly lower (around half). Figure 21B shows a very interesting feature of the estimated values for z_0 by the ensemble as predicted earlier in Figure 19, namely that the taken grid size seems to have no influence on the magnitude of the predicted values. In the ensemble, there is little directional dependency in the roughness estimate, as the values vary from 0.0085-0.0130m (absolute difference of 0.045m, relative difference of factor 1.53), though similar directional dependency as the Lettau algorithm portrayed earlier.
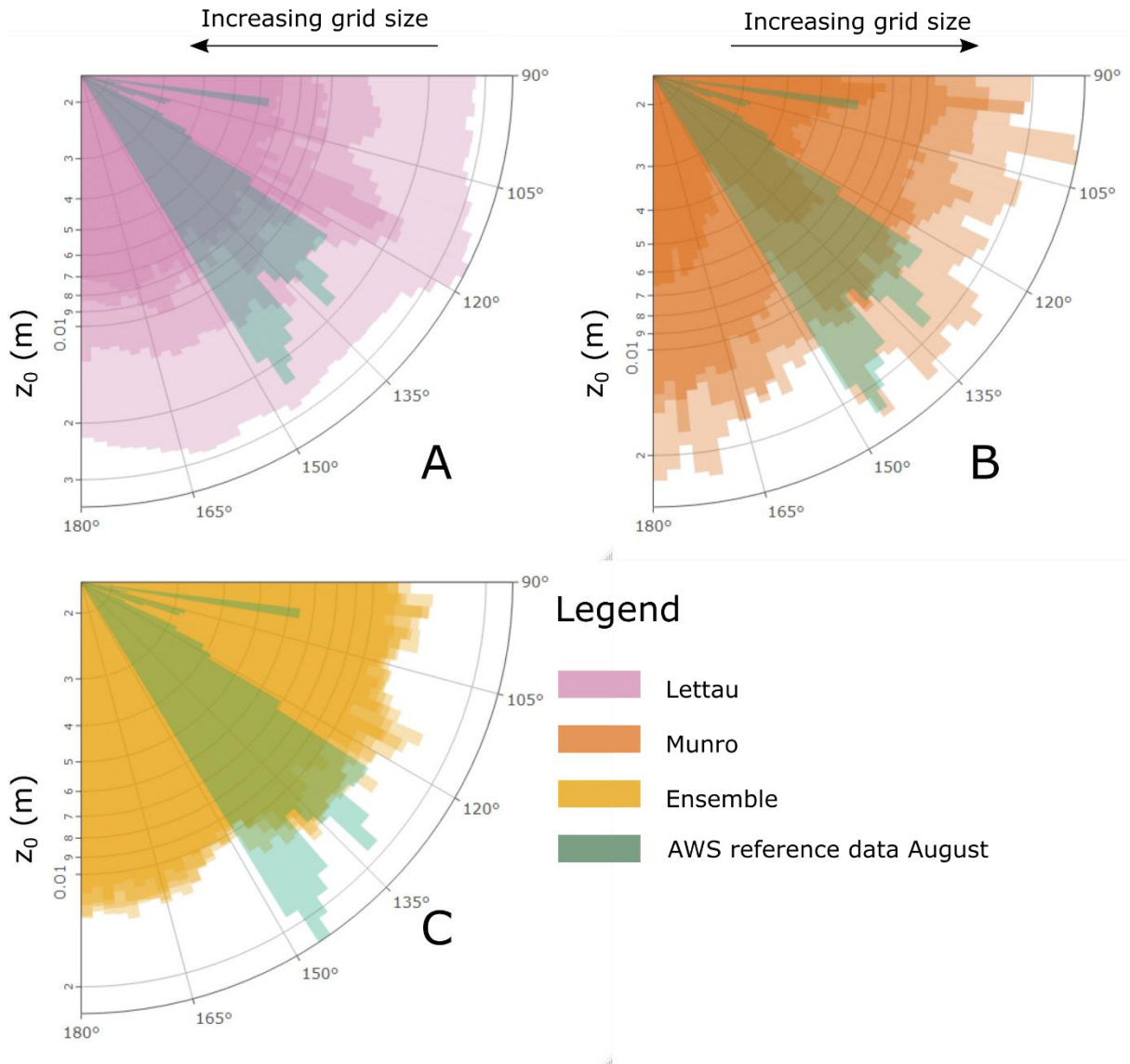
Figure 21. Results for the FG method using the Lettau (A), and Munro (B) algorithms and the Lettau-Munro Ensemble (C) for a grid size of 5, 10, 15, and 20m, which is illustrated by different shades. For Lettau applies the darker the shade, the higher the grid size. For Munro applies the lighter the shade, the larger the grid size. Within the ensemble almost no differences are discernible for the different grid sizes. The results are binned per 2 degrees, from 90-180°. The AWS reference data is of August 2019.

3.4.2 Nield

The Nield functions Nield SdElev and Max show great dependency on the chosen grid size, which can be observed in Figure 22. Both algorithms produce values of higher orders of magnitude as the grid size increases. For Nield SdElev the estimated roughness ranges from 0.012m at its lowest for grid size 5m, to 0.120m at its highest for grid size 20m, a factor 10 difference. The Nield Max estimated roughness has a similar range in values of a factor 10 difference between the lowest and highest produced value. The directional variability seems not affected by the different grid sizes, as the pattern of z_0 values seem to persist over grid size.
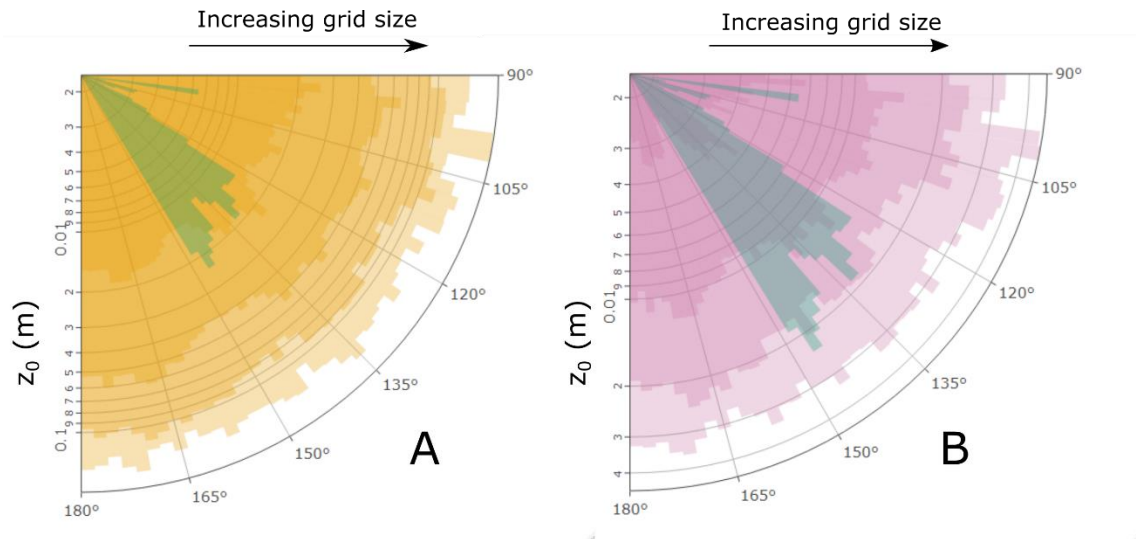
Figure 22. Results for the FG method using the Nield SdElev (A) and Nield Max (B) algorithms for grid sizes 5, 10, 15, and 20m, which is illustrated by different shades. The lighter the shade, the larger the grid size. The results are binned per 2 degrees, from 90-180°. The AWS reference data is of August 2019.

3.5 Turbulent flux estimation

The rationale of advancing our abilities to estimate the roughness is, as discussed in the Introduction, the need for improvement of flux estimation. Therefore, a simulation of the fluxes was made with the help of AWS data. The estimated z_0 values per direction were correlated to the wind direction, allowing us to use variable roughness over direction. The resulting simulated flux can be compared to the measured sensible heat flux by the AWS. Positive flux is defined upwards, which means that negative flux implies a heat flux towards the ice sheet (air temperature > surface temperature). As a multitude of parameters can be changed within both the FG and MF method, a selection was made to provide a clear comparison between methods. To show the influence of the grid size on the turbulent flux estimation by the FG method, the grid sizes 5m, and 20m are taken for both the Lettau and Munro, and the Nield algorithms. The influence of the footprint size is shown by comparing the simulated fluxes when using the z_0 estimate obtained by applying a 5x40m and a 15x200m footprint. Lastly, the influence of the DOF is examined by simulating the fluxes for one footprint (15x200m) and multiple DOF (6, 12, and 18). The chosen parameters are shown in Table 3.

Table 3. Parameters chosen for input roughness for the simulation of the turbulent fluxes

MF method	Footprint size	DOF of Spline	FG method	Grid size	Footprint size	Direction of transects
Lettau	5x40m, 15x200m	Not applicable to these functions	Lettau	5m, 20m	15x200m	x-direction
Munro	5x40m, 15x200m		Munro	5m, 20m	15x200m	x-direction
Ensemble	5x40m, 15x200m		Ensemble	5m, 20m	15x200m	x-direction
Nield SdElev	5x40m, 15x200m	6, 12, 18	Nield SdElev	5m, 20m	15x200m	x-direction
Nield Max	5x40m, 15x200m	6, 12, 18	Nield Max	5m, 20m	15x200m	x-direction

3.5.1 Using roughness values derived by the moving footprint method

Figure 23 shows the measured and simulated fluxes using the estimated z_0 by the MF method for the month August. Multiple key differences are discernible. First, from the figure it becomes apparent that most of the MF methods overestimate the measured flux regardless of footprint size. Then, the Nield functions are subject to large differences in magnitude as the footprint size increases. The 5x40m footprint results in mean fluxes of approximately -70 Wm^{-2} for Nield SdElev and -65 Wm^{-2} for Nield Max, while the 15x200m footprint results in mean fluxes of approximately -230 Wm^{-2} for Nield SdElev and -100 Wm^{-2} for Nield Max. A large portion of this difference can be attributed to the DOF of the spline function, which does not increase with increasing footprint size. The Lettau, Munro, and Lettau-Munro ensemble show much less sensitivity to footprint size. Furthermore, the simulated fluxes do produce a similar pattern for the whole time period. This is mainly since the roughness is only one parameter that is changed, and a large part of the pattern is formed due to the forcing data from the AWS. Additionally, it can be observed that the 5x40m footprints for Munro, Nield SdElev and Nield Max produce very similar results as is underlined by the violin plots of Figure 23C. Furthermore, it can be concluded that the Lettau method reproduced the measured flux best in this case, regardless of footprint size. It produces similar values to the measured flux, though overestimating or slightly underestimating it at times.

Figure 23. Simulated fluxes using the estimated z_0 of multiple MF techniques and AWS data of August (A). A single day has been highlighted (B) to provide a more detailed view, including a violin plot of the values of that single day (C).

3.5.2 Using roughness values derived using multiple DOFs

In Figure 24 the positive effect of increasing the DOF for the MF of 15x200m is clearly visible. The simulated fluxes using higher DOF yield results that match the measured flux more closely. The large peaks visible for Nield SdElev DOF = 6 are reduced for the other DOF. This is expected as the roughness values produced using higher DOF matched the measured z_0 more closely. Still, even with higher DOF, the simulated flux produced by the 5x40m footprint (Figure 23) with lower DOF are showing a closer resemblance to the measured flux.
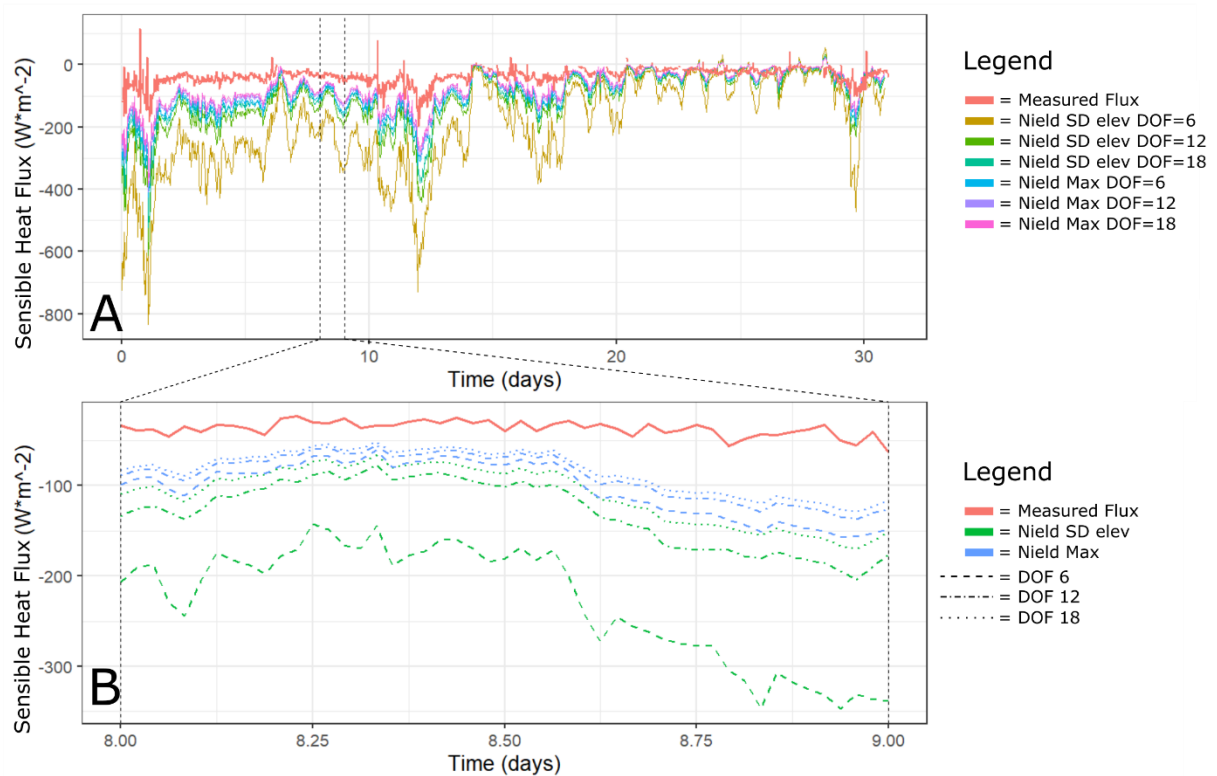
Figure 24. Simulated fluxes using the estimated z_0 of a 15x200m MF for Nield SdElev and Nield Max using multiple DOF and AWS data of August (A). A single day has been highlighted (B) to provide a more detailed view.

3.5.3 Using roughness values derived by the fixed grid method

Figure 25 shows the measured and simulated fluxes using the estimated z_0 by the FG method for the month August. From this figure it can also be concluded that the resulting z_0 values from the FG method also overestimate the measured flux in most cases. More interestingly, a difference in pattern can be observed for the FG and MF method. The magnitude of this overestimation is similar to the magnitude of overestimation of the MF method. The similarity between the patterns are also significant. The method that now best reproduces the measured flux, is the Munro algorithm with a grid size of 5m. This is underlined by comparing the mean estimated flux of Munro ($\pm$ -48 Wm^{-2}) to the mean measured flux ($\pm$- 37 Wm^{-2}). Still, this algorithm tends to overestimate the measured flux by 30%.
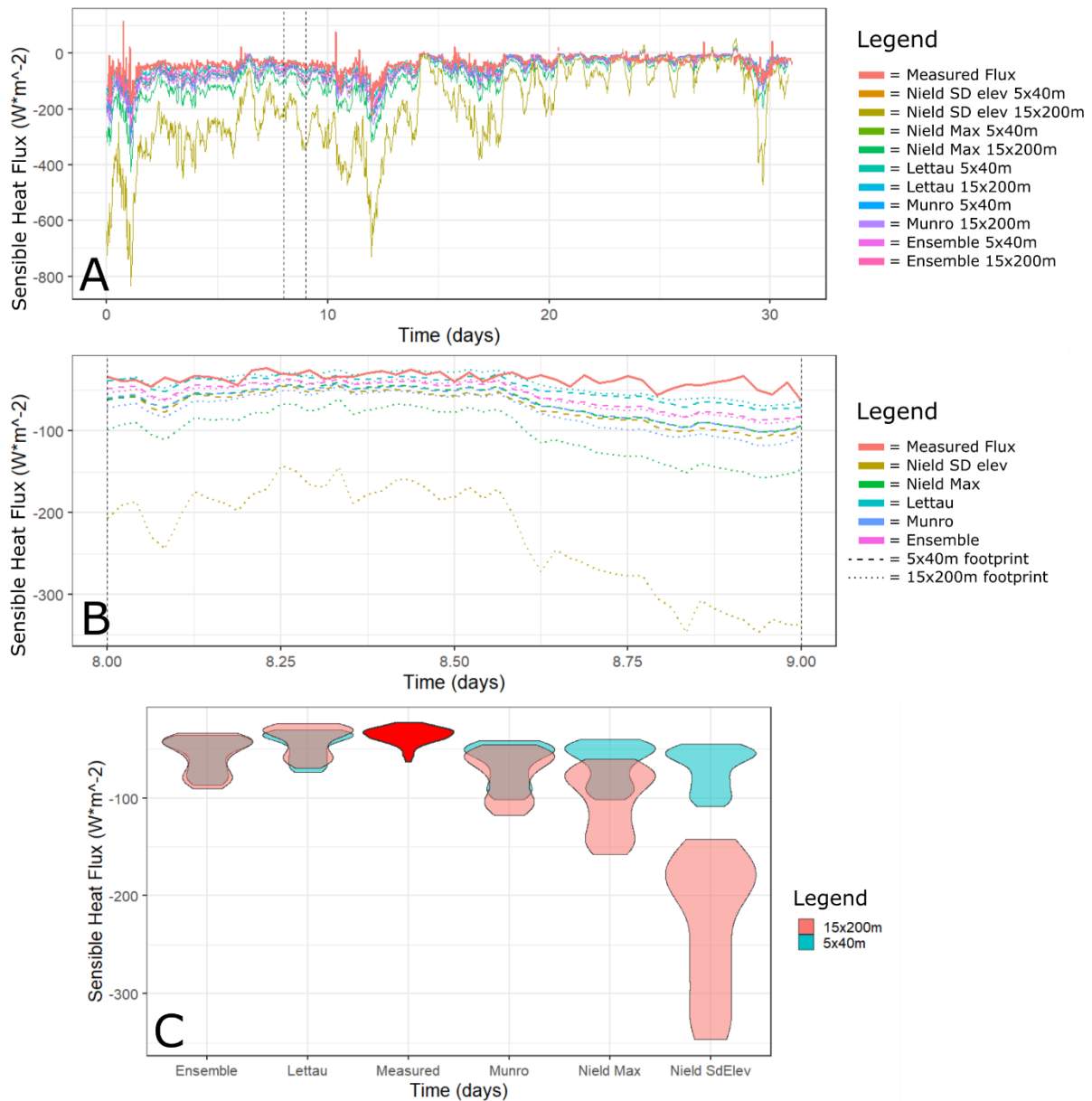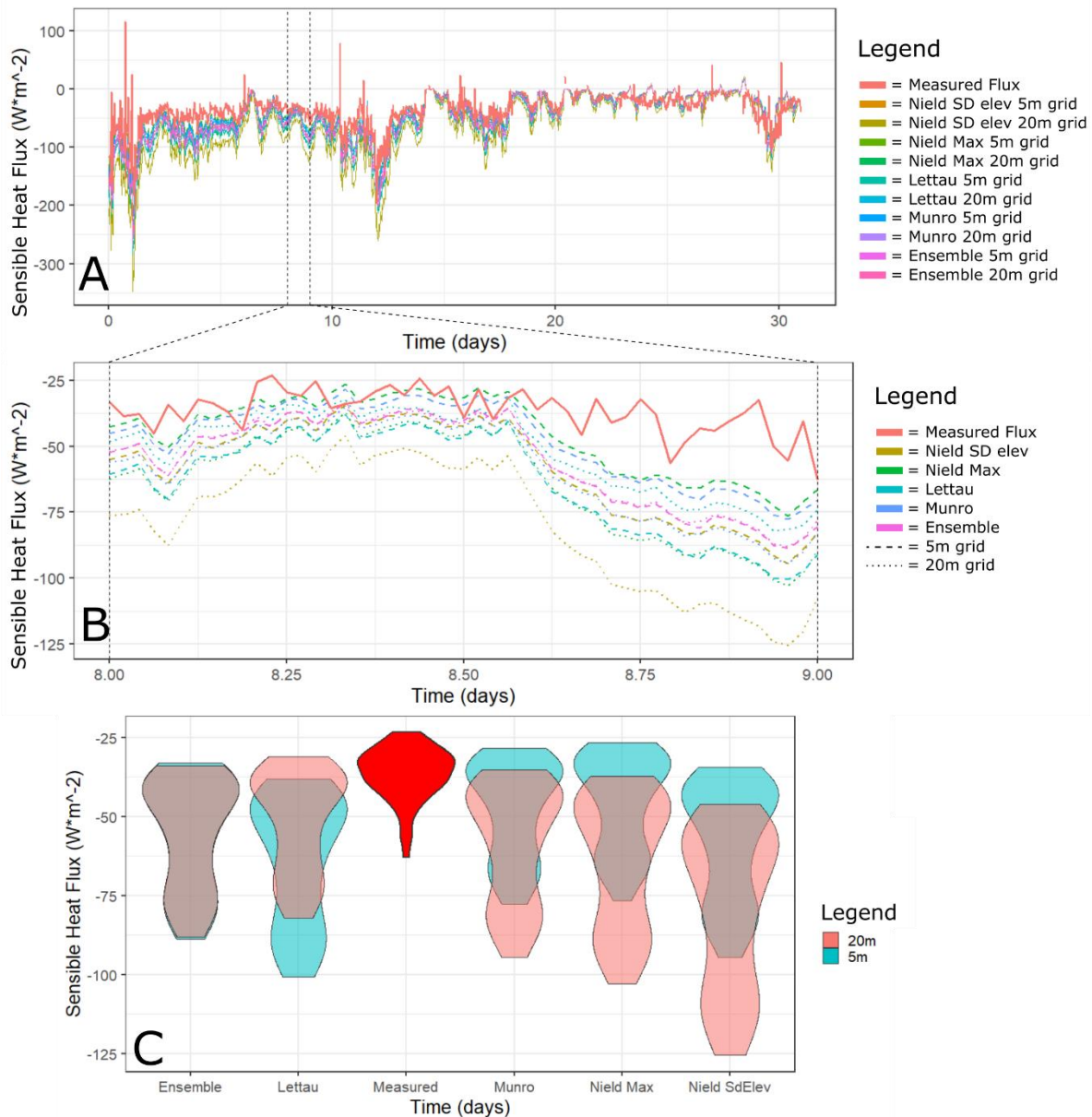
Figure 25. Simulated fluxes using the estimated z_0 of multiple FG techniques and AWS data of August (A). A single day has been highlighted (B) to provide a more detailed view, including a violin plot of the values of that single day (C).

3.6 Large scale RPAS imagery

No AWS was present for the area captured by the eBee flight; thus no reference data was available. This also applies to the KanM and KanL datasets. Therefore, it was decided to only produce FG results aiming to show the capability of this method to produce realistic z_0 estimates for multiple study areas spanning several magnitudes of size and resolution. From the KanM and KanL dataset, a subset was extracted for examination. One of the interesting aspects of assessing site A is that by visually assessing the DEM (Figure 11A) it can be expected that there will be higher roughness values for the southwest part of the plot area, as this is a relatively rough area dominated by crevasses. This should be captured in the FG results, as missing this feature would indicate weak performance of the FG method. Again, note that the scales are not identical for the different plot, which was done purposefully to compensate for methods with very low variability (e.g. Figure 26E+F).
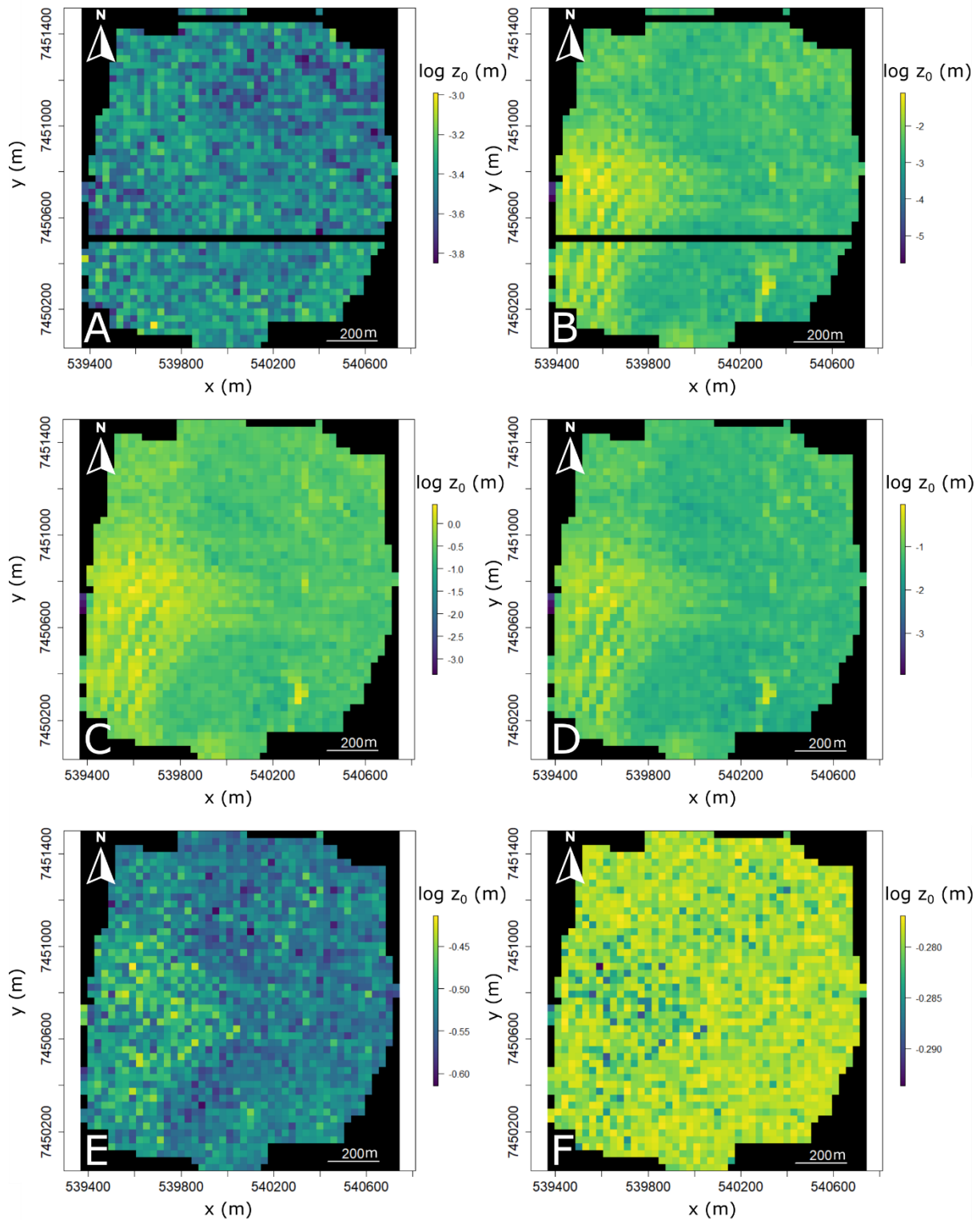
Figure 26. FG results with transects in x-direction at 30m grid size for methods: Lettau (A), Munro (B), Nield SdElev (C), Nield Mean (D), Nield SdObs (E), and Nield Max (F).

As we compare the different methods, multiple observations can be made. First, for most methods, the resulting estimated z_0 values are higher than the estimated z_0 values for site S5. Furthermore, most methods show sensitivity to the rough, crevassed area in the south-southwest. However, the Nield SdObs algorithm indicates that the area in this area is in fact slightly smoother (±-0.010-0.015m) than

the rest of the area. This is incorrect and further strengthens the believe that this algorithm can be excluded. Moreover, the Nield SdObs algorithm estimated z_0 does not differ from site S5, producing a range of values from ±0.505-0.530m against ±0.500-0.520m for site S5. Then, there is a striking similarity between the patterns produced by Munro, Nield SdElev, and Nield Max. These all clearly highlight the crevassed area as rough, as well as a smaller area around x=540300, y=7450250, while the rest of the area is rather uniform. Lastly, while it was expected that the Nield Mean would be underperforming, it was not expected for Lettau. As we examine the distributed results for the Lettau algorithm, it does not pick up the expected higher roughness in the crevassed area. Furthermore, there are no distinguishable features in the results; it resembles a uniform random distribution at best.
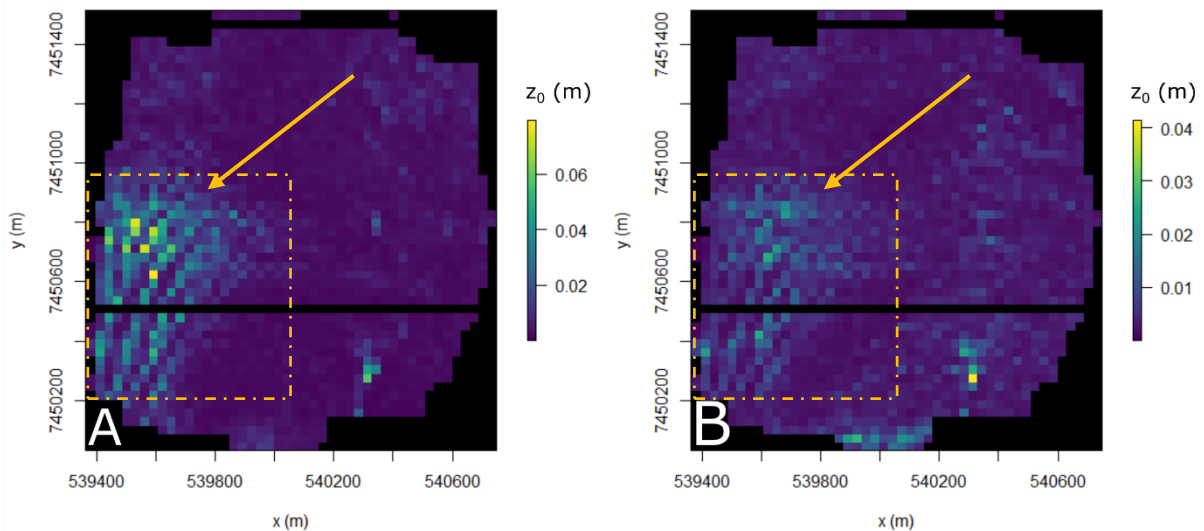
Figure 27. FG results using the Munro algorithm for site A at 30m grid size with taken transects in x-direction (A) and y-direction (B). Clearly visible is the higher roughness in the west-southwest. Also noticeable is the difference between the two directions; the transects in x-direction produce higher roughness values than transects in y-direction.

Another interesting aspect of the results is the clear difference between transects derived in x- and y-direction. As example are the FG results for site A shown in Figure 27 Here it is visible that while large parts of the site are estimated similarly, the rough area in the south-southwest is estimated differently. The transects in x-direction pick up higher roughness values than the transects in y-direction. This is due to the direction in which the features in this area are orientated, as is visible in Figure 11A. The main orientation of these crevasses is in north-south direction. This orientation complicates the capture of roughness by transects in equal direction. Transects perpendicular to this orientation, transects in x-direction, can capture this roughness quite easily. This will be further discussed in the section 4.4.4.
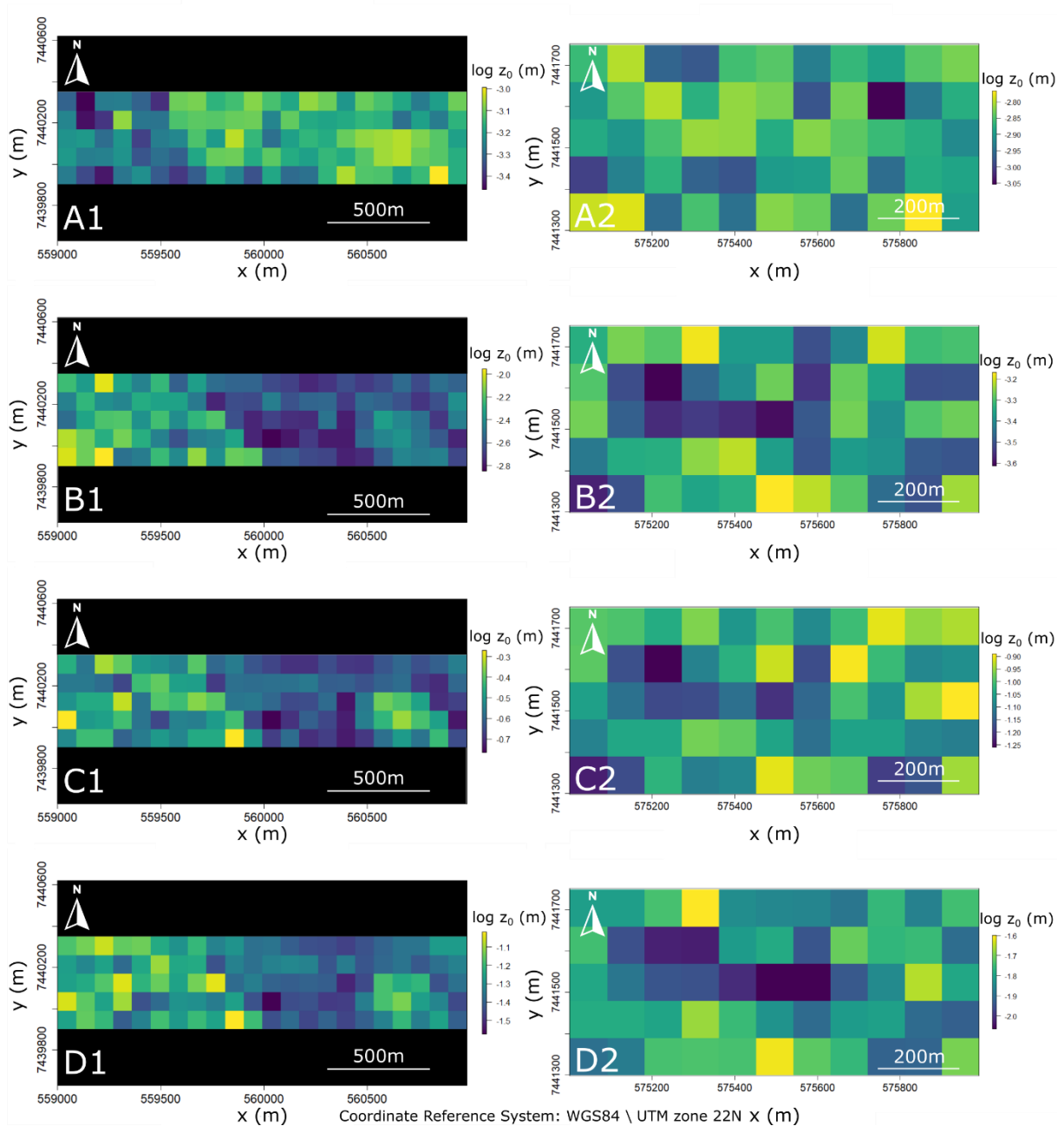
Figure 28. FG results for KanL (left column; 1) and KanM (right column; 2) at 90m grid size with transects in x-direction for methods Lettau (A), Munro (B), Nield SdElev (C), and Nield Max (D).

The KanL and KanM dataset show similar results regarding similarity of patterns; the Munro, Nield SdElev, and Nield Max algorithms produce similar patterns. The poor performance of Nield SdObs is also underlined, as again, it produces values between ±0.510-0.527m. Since it is extremely unlikely that the roughness of the different sites is of similar magnitude, Nield SdObs is deemed unsuitable when applied in this method. Importantly, this result shows that the methods pick up lower roughness values for KanM which is situated higher up on the ice sheet, where lower roughness values are expected. In the KanL dataset, this is even seen in a single plot as the roughness values decrease in eastern direction.

4. Discussion

4.1 Performance of Moving Footprint

The Moving Footprint technique makes use of the Lettau and Munro algorithms similar to their intended use; transects in a certain direction that provides us with a roughness estimate along the predominate wind direction. Therefore, it is not unexpected that this approach results in the best roughness estimates, as they reproduce great directional variability and result in estimated z_0 values in similar order of magnitude as the reference values. While the algorithms Nield SdElev and Nield Max also reproduce the directional influence, they do tend to overestimate the roughness. Even so, the capture of directional influence by both algorithms is a great benefit of this technique. Furthermore, directional influence is best captured by a smaller footprint. Additionally, this method is easy to apply, and does not require much computational power. Therefore, it can be of use for creating quick roughness estimates dependent on direction for a designated location, such as an AWS or other point of interest. The different footprint sizes are of influence on the resulting estimated z_0. Possibilities to ameliorate the tweaking of the footprint sizes are given later in section 4.4.2. It should be noted that the Nield SdObs and Nield Mean function do not produce realistic results in the MF method. The results show no directional variability, and the values do not correspond in magnitude to the reference values. Therefore, it is concluded that the Nield SdObs and Nield Mean functions are of no use for the MF technique, and should therefore not be considered. The main shortcoming is its inability to produce distributed roughness estimates, and therefore being unsuitable for larger datasets or for mapping the roughness of an area.

4.2 Performance of Fixed Grid

In contrast to the MF method, the FG method is able to produce distributed roughness estimates and can therefore be used to map the roughness of a complete area, and as a result provide insight in the spatial variability of roughness. It succeeds in this, as is exemplified by e.g. Figure 27, for which one glance is enough to observe the rough area in the south-southwest. Furthermore, it can capture variation of z_0 on a larger scale which is exemplified by the results for KanM and KanL where it picked up lower roughness values higher up the GrIS.

While the empirical Nield SdElev and Nield Max algorithms were developed to produce roughness estimates for flat, small (12x12m), square plots (Nield et al., 2013), they also seem to perform well on grid sizes of up to 90 times that cell size (90x90m plots, 8100m^2). While the values may be an overestimation at most times, it does produce great spatial results. The overestimation of values can be the result of an insufficient DOF of the spline detrending function. This will be discussed further later in section 4.4.1.

The mechanical algorithm of Lettau does not seem to perform well in the FG workflow. While the values are not far from expected, the spatial patterns show that very little spatial variability is captured, and roughness elements are not captured or distinguishable. The Munro algorithm however does work well in the workflow, as this captures roughness features such as crevasses, melt-water valleys, and other spatial objects. The Lettau-Munro ensemble does seem to produce viable results. However, this is probably mainly due to the influence of the Munro results, and while it produces results independent of grid size, it is unlikely that this ensemble is in fact a realistic option.

As mentioned, the Lettau-Munro ensemble produces results independent of grid size. This is also the case for the Nield SdObs and Nield Mean functions, yet these functions are not further discussed as we have seen that they did not perform well. All other functions have strong dependence on grid size. The Munro, Nield SdElev, and Nield Max roughness estimates all increase continuously as the grid size increased. The Lettau roughness estimate showed a contrasting trend; the roughness estimate

decreased continuously as the grid size increased. The FG in combination with a mean with Moving Footprint is also capable of producing results that contain some directional influence. Even so, the magnitude of the directional influence is much less than what the MF can produce. This is expected as transects are taken only in two directions (x- and y-direction, instead of all possible directions of the MF). Nevertheless, it is promising to see that some directional influence is retained even in the FG approach.

Another interesting result is the similarity of patterns in produced z_0 between the Munro, Nield SdElev, and Nield Max algorithms. The resulting orders of magnitude for estimated z_0 were also comparable between the Lettau and Munro versus the Nield algorithms. This in contrast to previous papers in which the resulting z_0 estimate often differed with (at least) an order of magnitude (Miles et al., 2017). The main cause why the resulting z_0 estimates are more alike, is the use of spline detrending instead of (bi)linear detrending which was used in the aforementioned paper. The bilinear detrending method does not sufficiently remove trends when applying the empirical Nield functions on larger scale. Spline detrending is proving to be a viable option.
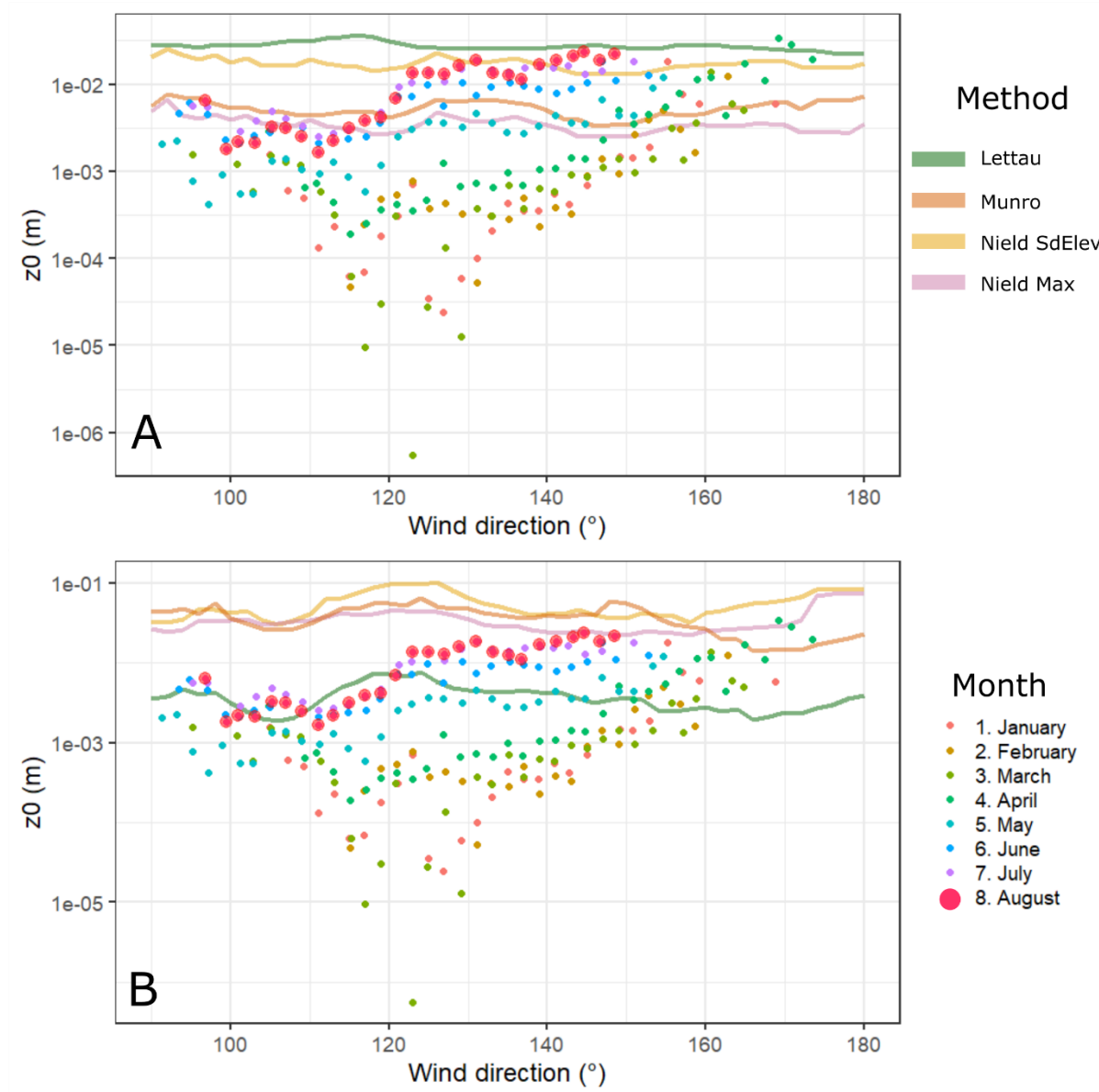

Figure 29. Reference z_0 values from the period January-August 2019 to put the resulting estimates for the FG (5m) (A) and MF (5x40m) (B) into perspective.

While solely focussing on the absolute reference values, it is also important to put the roughness estimates into perspective. Figure 29 shows the variability of z_0 over half a year as captured by the AWS including the estimate roughness values using the FG method (A) and the MF method (B) for selected algorithms. This shows that the z_0 itself varies over direction and time and can range from 0.00001 to 0.05m. This also stresses the difficulties related to roughness estimates, as the techniques should be capable of recreating roughness values in varying orders of magnitude.

4.3 Implications for flux estimation

After the assessment of the resulting turbulent flux estimation, and comparison to the measured flux, it was concluded that the simulated fluxes overestimate the measured flux. This could be detrimental to the results of this study, though a nuance should be made. While a comparison was made to the measured flux, which is the absolute benchmark, there was no comparison made to the relative benchmark; the turbulent flux simulated using the roughness values as obtained by the AWS. Therefore, we compared the best performing MF (Lettau, 5x40m) and FG (Munro, 5m) approaches to three measured z_0's (raw measured z_0, z_0 with an applied 12-hour Moving Average Focal (MAF) and z_0 with an applied 24-hour MAF) (Figure 30).
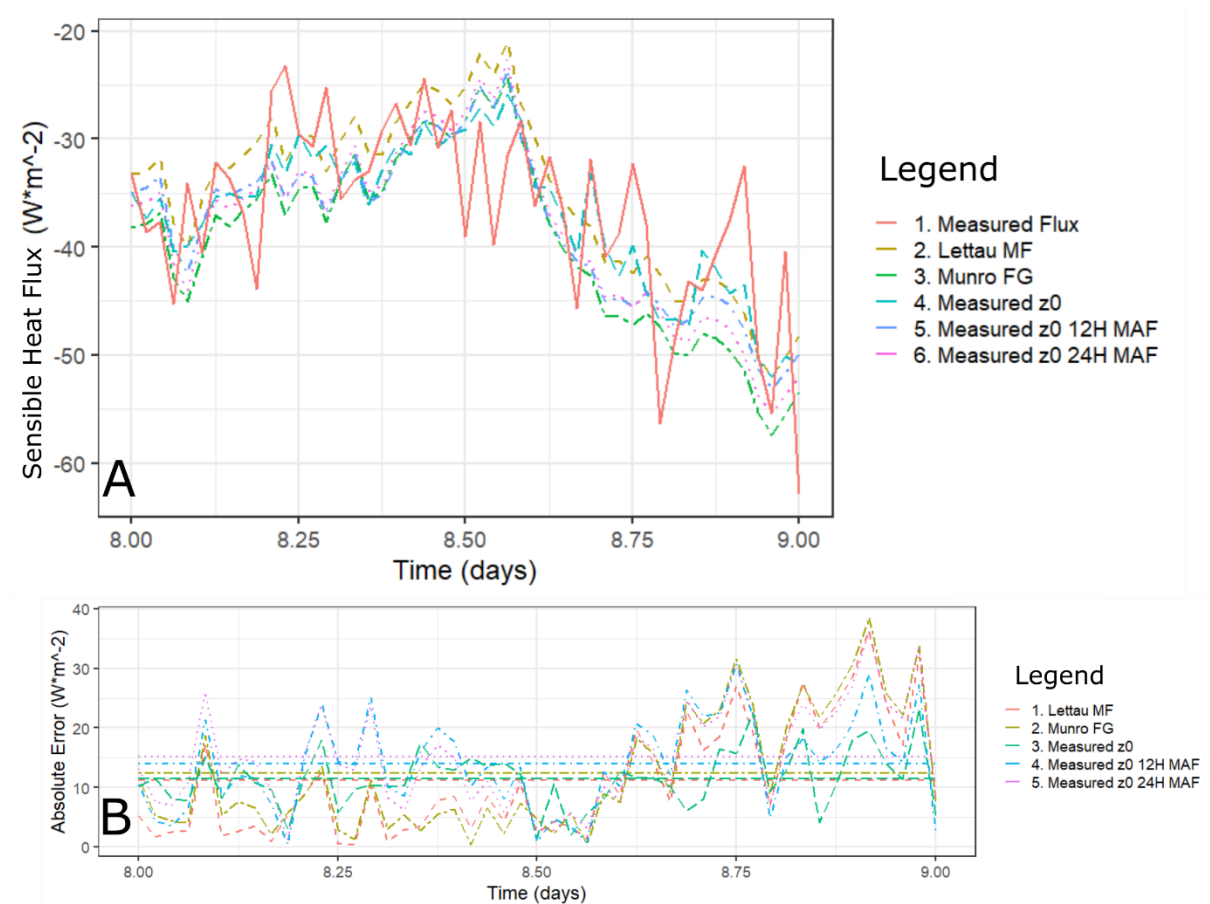
Figure 30. A comparison of simulated fluxes using estimated z_0's and simulated fluxes using measured z_0's (raw, 12-hour MAF and 24-hour MAF), taking the measured flux as a reference (A). In B the absolute errors are given including the mean per method.

Assessing Figure 30A reveals immediately that the simulated fluxes with measured z_0 values do not perfectly reproduce the measured flux. These simulated fluxes also tend to overestimate the actual flux by 11.5-15.2 Wm^{-2} on average (Figure 30B). In fact, they overestimate the measured flux to similar magnitude as the Lettau MF (mean absolute error = 11.2 Wm^{-2}) and Munro FG (mean absolute error = 12.4 Wm^{-2}) methods. This puts forth two main conclusions. The first conclusion is that the developed

methods seem to produce promising results and are thus a viable option for roughness estimation for large scale applications using high-resolution DEMs for the purpose of estimating turbulent fluxes. The second conclusion is that difficulties remain in simulating turbulent fluxes, as even simulated fluxes with measured roughness values do not perfectly reproduce the measured turbulent flux.

4.4 Limitations, simplifications, and recommendations

The developed methods were produced in such a fashion that the resulting required computational powers would be limited. For this purpose, some simplifications were made which may have resulted in imprecisions. In this part some simplifications are addressed, as well as their possible improvements for future purposes for when limitations regarding e.g. computational power may be removed.

4.4.1 Spline detrending

As stated in section 2.6.2, a spline detrending method was used prior to applying the empirical Nield algorithms. Since one of the objectives of this study was to determine a method suitable for larger datasets, focus was put on simplicity. Therefore, a single DOF was used of 6. This DOF was chosen manually after checking a multitude of areas and transects. While this simplified the process, it will most likely result in less consistent results for the Nield algorithms. The reason for this is that almost all surfaces are non-uniformly or irregularly shaped. Therefore, while a spline with a DOF of 6 will suffice for parts of the study area, for some other parts it may be too strict as there are large scale topographic differences; for other parts it may be too forgiving as there are little large scale topographical differences. Additionally, increasing the DOF will naturally result in a better fit, thus lower residuals. This will in turn produce lower roughness values as the lower the input statistics in the empirical functions, the lower the resulting output. Furthermore, when considering greater grid sizes, the DOF did not change in this study. It may be worthwhile to take greater DOF for greater grid sizes. A more elegant strategy should thus be adopted for choosing the DOF or in the appliance of the spline detrending.

In the current state of the developed methods, the detrending method is applied to the 1D transects, even within the FG method. The resulting consequence is that all transects within a grid have different splines. While it is unexpected that this causes erroneous results, future research could include the assessment of applying the spline detrending step using different approaches. This could be for example implementing a variable DOF by relating the DOF to certain surface characteristics. Other approaches can include detrending the individual grid blocks, or even the complete study area with a single spline function. To conclude, more research should be put in the performance of the spline detrending method before they are applied on larger scale.

4.4.2 Shape and size of footprint

The shape and size of the footprint mainly influences the results of the Moving Footprint method, in this case the results for S5. As the area of that was captured by the drone was limited, the option to vary the footprint size was also limited. The largest footprint that could be taken was the 15x200m footprint, as taking a larger footprint would result in reaching the limits of what has been documented by the RPAS. This footprint size was thus the upper limit of what was possible to assess in this study. The lower limit was arbitrarily set on 5x40m. These different footprint sizes are 'guesstimates' and may be unrepresentative. More research could focus on what footprint size is appropriate for AWS on the GrIS. Furthermore, it is known that the shape of a flux footprint is not a rectangle, but resembles more an oval shape (see Figure 31). While the rectangle may provide a good approximation, better would be to draw the transects in a manner similar to Figure 31C. However, getting this footprint right is difficult, and requires many parameters. Research shows promising developments in reducing the problems and required computational power related to creating flux footprint models as simple two-dimensional footprint parametrisations are being developed and tested (Kljun et al., 2015).
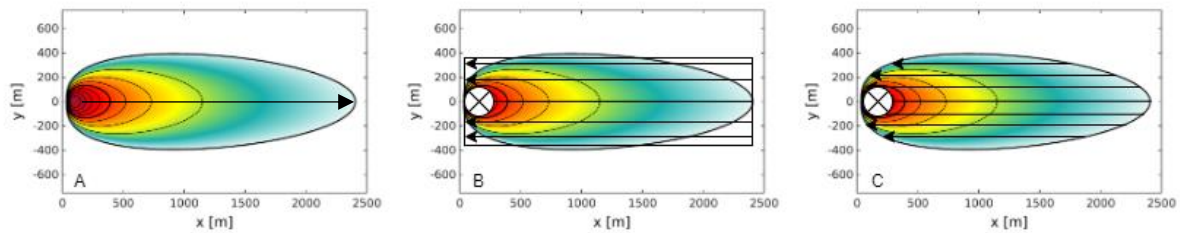
Figure 31. An example of a 2D footprint estimate (A), which in the current method is approximated by a rectangle in which transects are taken (B), but which could be ameliorated by applying the transects as drawn in C. The crossed circle represents the AWS location. The footprint contour lines are shown in steps of 10% from 10 to 90% (increasing in the direction of the arrow in A), also correlating to the colour which denotes the relative contribution of the area to the total footprint. Original footprint after Kljun et al., (Kljun et al., 2015).

The footprint also influences the Fixed Grid method since the Moving Footprint calculates the mean per footprint is applied over the FG distributed results. Now, each cell is given equal weights. However, as is also depicted in Figure 31, the area near the AWS influences the aerodynamics more than an area further away. It may be possible that this should be accounted for in the MF over FG step. Future research could explore the possibility of adding variable weights to the individual grid cells.

4.4.3 Dome-effect

The DEMs for the sites S5 and A were created without the help of GCPs, which can cause a significant dome-effect (Eltner and Schneider, 2015). This can be checked by verifying the created data with verified elevation data e.g. an IceSat2-track. However, as the profiles are detrended this possible effect was neglected since detrending the profile would remove the aforementioned effect in any case. While this is certainly the case when using the spline detrending method, it may not be the case for the linear detrending method, as the dome shape is a parabolic; fitting a straight line through a parabolic shape is problematic. Therefore, the possible influence of the dome-effect on the Lettau and Munro roughness estimates should be examined. It is not expected that the dome-effect in this study is of minor influence, as visual inspection did not reveal a dome-structure in the DEM.

4.4.4 Transect direction

Step 2 of the FG method (Figure 10) states that the 2D grid cells were divided into 1D transects in x- and y-direction. This results in transects in only two directions, which in contrast to the MF method wherein you can theoretically obtain transects in 360 different directions, shows a significant shortcoming. When the FG method is applied to anisotropic surfaces (i.e. surfaces which are formed in certain direction), this anisotropy can only be captured when the direction of the anisotropy correlates to the direction of the transect as is depicted in Figure 32. Now, the FG method is only capable of working in the x- and y-direction. This while it is known that some parts of the GrIS are shaped in the direction of the predominant wind direction, and crevasses can also be found in certain directions, exemplifying the anisotropy of the GrIS (Smith et al., 2006). Therefore, we recommend that prior to applying the FG method in the current state, isotropy should be established. Furthermore, future enhancements of the method could include the possibility of multi-directional transects construction. It is an option to combine the MF and the FG methods developed in this paper to create said functionality, though this would require far more computational power than the two separate methods, therefore it was left out as it was not in the scope of this research. A simple solution that requires (almost) no additional coding, is rotating the elevation raster in such fashion that the direction of the anisotropy (if present) is in the same direction as the x-axis or y-axis. This results in the highest roughness value for the study area. Another option is rotating the elevation raster in such a way that

the transects are taken in the direction equal to the main wind direction. This results in a representative roughness for the study area, as it is not necessarily that the anisotropic direction is equal to the main wind direction. This way, it is expected that the current method and code can be used to produce meaningful results for anisotropic surfaces.
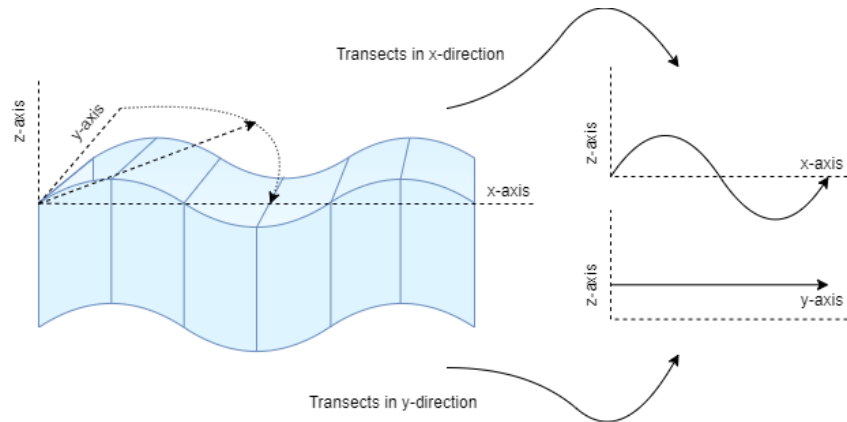

Figure 32. An extreme case of anisotropy; a sinusoidal wave. When applying the FG method and constructing transects in x- and y-direction, the transects in y-direction do not capture any variability in elevation, while transects in x-direction do capture variability in elevation. Within these extremes the variability increases as the angle between the transect and the y-axis increases, until the point the line coincides with the x-axis.

4.4.5 Moving focal option

One of the advantages of the FG method, is also one of its disadvantages. The FG method calculates a roughness value per grid tile (computationally easy). As the grid tile is in the case of this study at least 200 times larger than the original resolution, the resulting map will consequently have a lower resolution as the original input map. This may not be desired in some cases. A future development of the method that involves the application of a moving focal function could be a solution to retain the original high-resolution data. Currently, this moving focal is not a feasible option as run times will increase dramatically compared to the Fixed Grid method. While the Fixed Grid method took about 8 hours to complete when processing the entire S5 site, the moving focal took 7 days for a small section (±50x50m) of S5.

4.4.6 Use of satellite data

Future research could also focus on the use of high-resolution satellite data. One new source of interesting data is the Advanced Topographic Laser Altimeter System (ATLAS) onboard the ICESat-2 satellite. The ATLAS is an, with respect to the ICESat-1/GLAS measurement system, improved dual-beam single-photon counting laser altimeter (Abdalati et al., 2010; Neumann et al., 2019). Each beam has a 17m spatial footprint diameter with 0.7m along-track spacing and can provide sub-decimal elevation change. While this satellite gives great new prospects with regards to elevation changes of the GrIS, the nature of the data provides some difficulties when the methods developed in this paper are applied. Since the data is extracted in beams, it is possible only to create a few transects and only in the direction of the beam. While these transects can be used as input for the algorithms, their use is limited as only one direction can be considered. While an aerodynamic roughness estimate can be produced for isotropic surfaces, for anisotropic surfaces this is not achievable.

4.4.7 Most appropriate method for the Greenland Ice Sheet

Multiple methods have been presented in this paper, all with their own strong and weak points. It is highly interesting to see what works best. However, it is possible that for different study areas, different combinations of grid sizes, resolutions and techniques produce best results. Therefore, a recommendation is made how to determine the approach to produce best roughness values for an area with no reference data to check. First, the area should be checked on its isotropy. If the study area is uniformly variable in all directions, the Fixed Grid method can be applied in its current state, as the direction of the transects will not influence the roughness estimate. Vice versa, when the directions of the transects have an influence on the roughness estimate, you will know that the area shows anisotropic features. If the study area contains anisotropic features, it should be decided whether to draw transects in anisotropic direction or in main wind direction. This can be achieved by rotating the entire raster so that the rows or columns are in the same direction as intended. Then, a representative point should be taken, which will act as a dummy AWS. Hereafter transects from possible wind directions should be taken to this dummy AWS location for an appropriate footprint. The transects are then fed into the Lettau algorithm, as this method produced roughness values that matched most closely to the reference data. The roughness values estimated by the MF Lettau will then act as anchor point for the other values. Hereafter, the whole study area is considered using the FG technique and the Munro, Nield SdElev, and Nield Max algorithm, as these algorithms proved to capture spatial variability on both smaller and larger scale. The size of the grid cells, and thus transects, should ideally be in the order of metres when the resolution is in centimetres, as has been proposed in earlier papers (Rees and Arnold, 2006). This paper found that roughness is reasonably well described by scale-free models longer than a few metres, and shorter than about 100m. This fractal behaviour was established for a snow-free surface of a glacier in Svalbard, and not for the GrIS. Therefore, more research can point out whether assumption and underlying relation holds for the GrIS. Anyhow, in this paper the relation boils down to 2.5cm resolution - 5m grid size, 30cm resolution - 30m grid size, and 60cm resolution - 90m grid size. In practice, a ratio of 1:100 to 1:200 should be maintained. Then the resulting values are compared between the FG and MF methods, with the MF values providing as an anchor as to what order of magnitude should be expected. The final step is checking the difference in magnitude between the FG and MF, and possibly adjusting the values for the FG distributed results.

4.5 Relation z_0 and wind speed

It is important to establish whether the wind speed has an influence on the z_0 measured by the AWS. Primarily since the possible presence of a relation between wind speed and z_0 implicates that certain roughness elements are only captured by larger footprints. This would mean that upwind of the AWS, certain roughness elements are located that are included in the measured z_0 if the wind speed is sufficiently high, so that the roughness elements are located within the footprint. Second, the z_0 estimates that were produced in this study did not take wind speed into account. Might there be a relation between z_0 and wind speed, this should be accounted for. Therefore, a scatterplot was made to examine the possible relation between the aforementioned two factors which is presented in Figure 33.
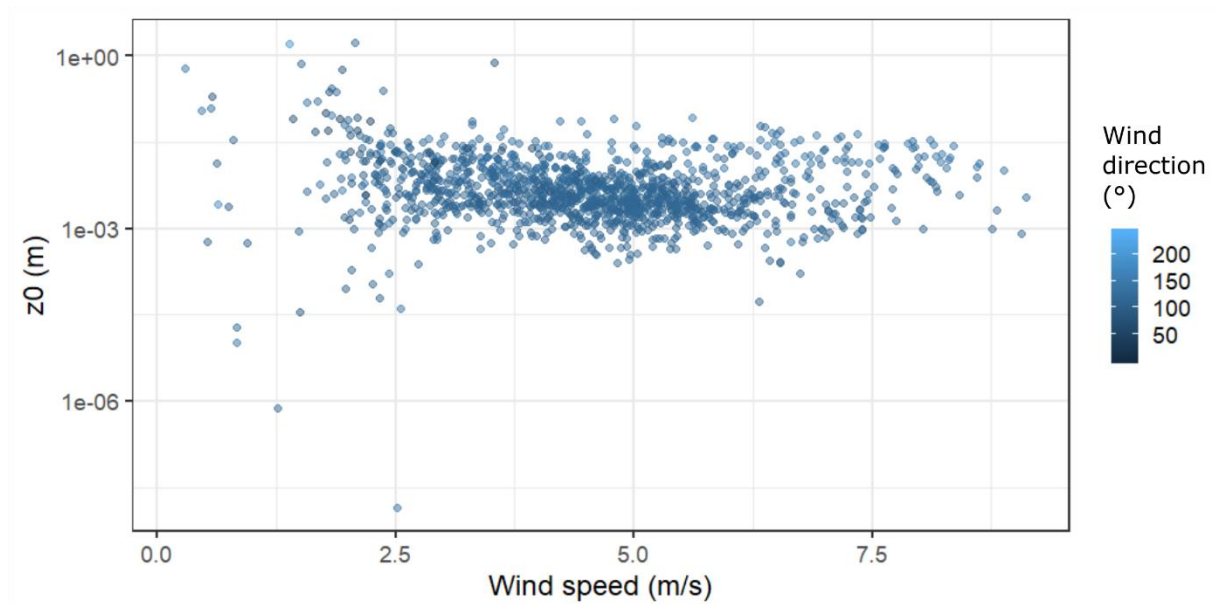
Figure 33. Scatterplot of wind speed against measured z_0 by the AWS of S5 for the month August.

This scatterplot does not show a relation between wind speed and z_0. The implication of this absence of relation is that there are no roughness elements upwind of the AWS that are only captured at higher wind speed. In other words, the AWS is not located in the wake of a roughness object that is only captured at higher wind speeds. While this is desired for the location of an AWS, it is not always achieved as you are limited by the possible locations to place an AWS by for example accessibility of the site. For this paper, it strengthens the belief that the documented area is of sufficient size to provide meaningful roughness estimations in the directions from 90-180°.

4.6 Relation original DEM resolution on z_0

Figure 34 shows the mean estimated aerodynamic roughness plotted against the original resolution of the DEM. To create this figure, the original DEM of site S5 was coarsened from 2.5cm to 5, 50, 100, 250 and 500cm. Then, the Moving Footprint method was applied to determine if and what the influence of the resolution on estimated z_0 is. From the figure can be concluded that there is a negative relation between resolution and z_0 estimate; the coarser the resolution, the lower the estimated z_0. This link is visible for both Lettau and Munro. This relation can be explained by the loss of roughness elements by coarsening the resolution, as small variations in elevation are averaged out by this step. Interesting is that the slope at which both the algorithms decrease looks similar, while the values of both algorithms differed significantly in magnitude. From the figure it can be concluded that a (negative) logarithmic relation can be established. Whether this logarithmic relation is coincidence, or that this relation holds for other areas as well can be an opportunity for future research.
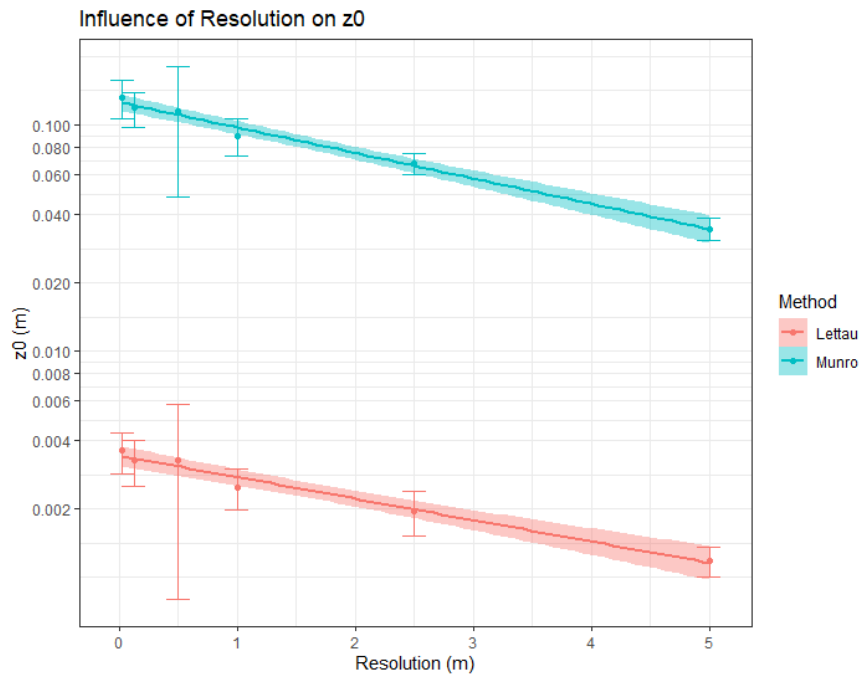
Figure 34. Plot of mean z_0 values with standard deviation against resolution of original DEM over which the moving footprint (15x200) was applied, with a fitted linear model and 95% confidence interval.

5. Conclusion

This study showed that RPAS-derived DEMs of various scales and resolutions can be used to produce realistic topographic roughness estimates by applying a variety of microtopographic methods and comparing the resulting estimates to values obtained by aerodynamic inversion of AWS data. Both of the in this study developed methods, the Fixed Grid method (FG) and the Moving Footprint method (MF), produced promising results in combination with the Lettau (Lettau, 1969) and Munro (Munro, 1989) algorithms, and the Nield (Nield et al., 2013) functions. These methods resulted in roughness estimates approximating the reference values obtained by aerodynamic inversion of AWS data, though overestimating it in most cases.

When comparing the FG and the MF method the following findings are important. The MF worked especially well in combination with the Lettau equation, producing roughness estimates close to the reference values. Furthermore, the MF also proved capable of partly reproducing the high dependency of the roughness on the prevalent wind direction. Additionally, the MF requires low computational power and is easy to apply. As a result, it is suitable for producing directional dependent roughness estimates for a specific location. In contrast, its main shortcoming is the inability to produce distributed roughness estimates.

The FG method proves that it can produce realistic distributed roughness estimates and roughness patterns, complementing the MF method. Spatial patterns were reproduced by multiple algorithms. The largest similarity in patterns was exemplified by the Munro, Nield SdElev, and Nield Max algorithm. While the Lettau algorithm performed well in the MF method, it underperformed in the FG methodology, as it did not reproduce spatial patterns. The Nield algorithm that makes use of the standard deviation of obstacle height, in this study continuously referred to as Nield SdObs, is proven unable to produce realistic results in both FG and MF methods. It produces no variable results, as the z_0 estimate ranges from 0.50-0.55m for each plot regardless of input. Visible assessment of roughness patterns has confirmed the poor performance. Hence, the Nield SdObs algorithm can be excluded from further research. The Nield equation that makes use of the mean obstacle height (Nield Mean) is able to reproduce some of the spatial patterns, yet structurally overestimates the values by an order of magnitude. Therefore, this algorithm can also be excluded from further research. To conclude, the FG method is a computational inexpensive method capable of producing realistic distributed roughness estimates and roughness patterns. The algorithms that perform well inside the FG method are the Munro, Nield SdElev, and Nield Max algorithms. These also shown capable of capturing variability in z_0 on a larger scale, exemplified by the studies of KanL and KanM.

The impact of spatial scale on the aerodynamic roughness by the FG method is considerable. The roughness estimates of almost all algorithms are dependent on the chosen grid size, with an exception for Nield SdObs and Nield Mean. For most algorithms, the following statement applies: the larger the grid size, the larger the estimated roughness length for momentum. The estimated roughness length can multiply by a factor three to five when increasing the grid size of the FG from 5m to 20m, depending on what algorithm is used. Only Lettau showcases a negative relation between grid size and estimated roughness value. A logarithmic mean of the Lettau and Munro algorithms also proves to be independent on grid size. For the Nield equations, the grid size dependency may be partly caused by the fixed degrees of freedom (or number of nodes) of the spline function over the different grid sizes. Future research should examine the possibility of variable degrees of freedom per grid size.

The resolution of the input DEM also affects the aerodynamic roughness estimate. The coarser the original resolution, the lower the roughness estimate. The observed relation for the Munro and Lettau equation was that the modelled z_0 decreased logarithmically with coarser resolution. Whether this is coincidence or the possibility that this relation holds, is opportunity for future research.

This study also shows that it is possible to simulate the turbulent fluxes with relative high accuracy when using the produced roughness estimate. The best performing techniques were the Lettau MF method, the 5m FG method, and the 5m Nield Max which reproduced the turbulent fluxes with an average absolute error of 11.2 Wm^{-2} (Lettau), 12.4 Wm^{-2} (Munro), and 10.7 Wm^{-2} (Nield Max). The average absolute error of the simulated fluxes using roughness values obtained by the AWS amounted to 11.5 Wm^{-2} (Measured raw), 13.9 Wm^{-2} (Measured 12-hour moving focal average), and 15.2 Wm^{-2} (measured 24-hour moving focal average). This shows that the method can perform just as well as the simulated fluxes obtained by the AWS. Increasing the grid size will cause the absolute error to increase.

For users that are interested in applying the methods of this research to large scale datasets, it is recommended that a combination of the two methods is used. This study showed that a MF using the Lettau algorithm for a footprint of 5x40-15x200m in size moving over a high-resolution DEM (2.5cm) produces results that match the directional variability and the magnitude of the AWS reference data. The MF method using the Munro, Nield SdElev, and Nield Max algorithms at a small grid size (5m) for a high-resolution DEM (2.5cm) show spatial differences over the study area. By combining these techniques, an insight is given in the magnitude of z_0 and the variability over the studied area.

ICEsat-2 tracks are a good source of extra information and can provide additional verification of elevation data. However, as the satellite makes use of tracks in certain direction, it can only produce roughness estimates in a certain direction. Therefore, the ICEsat-2 tracks can only be used in a way similar to the FG method used in this paper if the surface that is considered is isotropic.

Future research can focus on more elegant ways to apply spline detrending in the Fixed Grid method. It can also explore to what extent the Moving Footprint can be improved by creating footprints more similar to realistic footprints, and adding weights to cells so that cells closer to the AWS are given more weight than cells further away.

6. References

Abdalati, W., Zwally, H.J., Bindschadler, R., Csatho, B., Farrell, S.L., Fricker, H.A., Harding, D., Kwok, R., Lefsky, M., Markus, T., Marshak, A., Neumann, T., Palm, S., Schutz, B., Smith, B., Spinhirne, J., Webb, C., 2010. The ICESat-2 laser altimetry mission. Proc. IEEE 98, 735–751. https://doi.org/10.1109/JPROC.2009.2034765

Andreas, E.L., Murphy, B., 1986. Bulk Transfer Coefficients for Heat and Momentum over Leads and Polynyas. J. Phys. Oceanogr. 16, 1875–1883. https://doi.org/10.1175/1520-0485(1986)016<1875:btcfha>2.0.co;2

Arnold, N.S., Rees, W.G., Hodson, A.J., Kohler, J., 2006. Topographic controls on the surface energy balance of a high Arctic valley glacier. J. Geophys. Res. 111, F02011. https://doi.org/10.1029/2005JF000426

Bamber, J.L., Westaway, R.M., Marzeion, B., Wouters, B., 2018. The land ice contribution to sea level during the satellite era. Environ. Res. Lett. 13. https://doi.org/10.1088/1748-9326/aac2f0

Belward, A.S., Skøien, J.O., 2015. Who launched what, when and why; trends in global land-cover observation capacity from civilian earth observation satellites. ISPRS J. Photogramm. Remote Sens. 103, 115–128. https://doi.org/10.1016/j.isprsjprs.2014.03.009

Benassi, F., Dall'Asta, E., Diotri, F., Forlani, G., Cella, U.M. di, Roncella, R., Santise, M., 2017. Testing accuracy and repeatability of UAV blocks oriented with gnss-supported aerial triangulation. Remote Sens. 9. https://doi.org/10.3390/rs9020172

Bevis, M., Harig, C., Khan, S.A., Brown, A., Simons, F.J., Willis, M., Fettweis, X., van den Broeke, M.R., Madsen, F.B., Kendrick, E., Caccamise, D.J., van Dam, T., Knudsen, P., Nylen, T., 2019. Accelerating changes in ice mass within Greenland, and the ice sheet's sensitivity to atmospheric forcing. Proc. Natl. Acad. Sci. U. S. A. 116, 1934–1939. https://doi.org/10.1073/pnas.1806562116

Bhardwaj, A., Sam, L., Akanksha, Martín-Torres, F.J., Kumar, R., 2016. UAVs as remote sensing platform in glaciology: Present applications and future prospects. Remote Sens. Environ. https://doi.org/10.1016/j.rse.2015.12.029

Bindschadler, R., 1998. Monitoring ice sheet behavior from space. Rev. Geophys. 36, 79–104. https://doi.org/10.1029/97RG02669

Bintanja, R., van den Broeke, M.R., 1995. The surface energy balance of Antarctic snow and blue ice. J. Appl. Meteorol. 34, 902–926. https://doi.org/10.1175/1520-0450(1995)034<0902:TSEBOA>2.0.CO;2

Bintanja, R., van den Broeke, M.R., 1994. Local climate, circulation and surface-energy balance of an Antarctic blue-ice area. Ann. Glaciol. 20, 160–168. https://doi.org/10.3189/1994aog20-1-160-168

Böning, C.W., Behrens, E., Biastoch, A., Getzlaff, K., Bamber, J.L., 2016. Emerging impact of Greenland meltwater on deepwater formation in the North Atlantic Ocean. Nat. Geosci. 9, 523–527. https://doi.org/10.1038/ngeo2740

Brock, B.W., Mihalcea, C., Kirkbride, M.P., Diolaiuti, G., Cutler, M.E.J., Smiraglia, C., 2010. Meteorology and surface energy fluxes in the 2005-2007 ablation seasons at the Miage debris-covered glacier, Mont Blanc Massif, Italian Alps. J. Geophys. Res. Atmos. 115, 9106. https://doi.org/10.1029/2009JD013224

Brock, B.W., Willis, I.C., Sharp, M.J., 2006. Measurement and parameterization of aerodynamic

roughness length variations at Haut Glacier d'Arolla, Switzerland. J. Glaciol. 52, 281–297. https://doi.org/10.3189/172756506781828746

Brock, B.W., Willis, I.C., Sharp, M.J., Arnold, N.S., 2000. Modelling seasonal and spatial variations in the surface energy balance of Haut Glacier d'Arolla, Switzerland. Ann. Glaciol. 31, 53–62. https://doi.org/10.3189/172756400781820183

Chappell, A., Heritage, G.L., 2007. Using illumination and shadow to model aerodynamic resistance and flow separation: An isotropic study. Atmos. Environ. 41, 5817–5830. https://doi.org/10.1016/j.atmosenv.2007.03.037

Chudley, T.R., Christoffersen, P., Doyle, S.H., Abellan, A., Snooke, N., 2019. High-accuracy UAV photogrammetry of ice sheet dynamics with no ground control. Cryosph. 13, 955–968. https://doi.org/10.5194/tc-13-955-2019

Cooper, M.G., Smith, L.C., 2019. Satellite remote sensing of the Greenland Ice Sheet Ablation Zone: A review. Remote Sens. https://doi.org/10.3390/rs11202405

Cuffey, K.M., Marshall, S.J., 2000. Substantial contribution to sea-level rise during the last interglacial from the Greenland ice sheet. Nature 404, 591–594. https://doi.org/10.1038/35007053

Cullen, N.J., Mölg, T., Kaser, G., Steffen, K., Hardy, D.R., 2007. Energy-balance model validation on the top of Kilimanjaro, Tanzania, using eddy covariance data, in: Annals of Glaciology. pp. 227–233. https://doi.org/10.3189/172756407782871224

Ding, Q., Schweiger, A., L'Heureux, M., Battisti, D.S., Po-Chedley, S., Johnson, N.C., Blanchard-Wrigglesworth, E., Harnos, K., Zhang, Q., Eastman, R., Steig, E.J., 2017. Influence of high-latitude atmospheric circulation changes on summertime Arctic sea ice. Nat. Clim. Chang. 7, 289–295. https://doi.org/10.1038/nclimate3241

Eltner, A., Schneider, D., 2015. Analysis of Different Methods for 3D Reconstruction of Natural Surfaces from Parallel-Axes UAV Images. Photogramm. Rec. 30, 279–299. https://doi.org/10.1111/phor.12115

Elvidge, A.D., Renfrew, I.A., Weiss, A.I., Brooks, I.M., Lachlan-Cope, T.A., King, J.C., 2016. Observations of surface momentum exchange over the marginal ice zone and recommendations for its parametrisation. Atmos. Chem. Phys. 16, 1545–1563. https://doi.org/10.5194/acp-16-1545-2016

Enderlin, E.M., Howat, I.M., Jeong, S., Noh, M.J., van Angelen, J.H., van den Broeke, M.R., 2014. An improved mass budget for the Greenland ice sheet. Geophys. Res. Lett. 41, 866–872. https://doi.org/10.1002/2013GL059010

Fausto, R.S., As, D., Box, J.E., Colgan, W., Langen, P.L., Mottram, R.H., 2016. The implication of nonradiative energy fluxes dominating Greenland ice sheet exceptional ablation area surface melt in 2012. Geophys. Res. Lett. 43, 2649–2658. https://doi.org/10.1002/2016GL067720

Fettweis, X., Franco, B., Tedesco, M., van Angelen, J.H., Lenaerts, J.T.M., van den Broeke, M.R., Gallée, H., 2013. Estimating the Greenland ice sheet surface mass balance contribution to future sea level rise using the regional atmospheric climate model MAR. Cryosph. 7, 469–489. https://doi.org/10.5194/tc-7-469-2013

Fitzpatrick, N., Radić, V., Menounos, B., 2019. A multi-season investigation of glacier surface roughness lengths through in situ and remote observation. Cryosphere 13, 1051–1071. https://doi.org/10.5194/tc-13-1051-2019

Fonstad, M.A., Dietrich, J.T., Courville, B.C., Jensen, J.L., Carbonneau, P.E., 2013. Topographic

structure from motion: A new development in photogrammetric measurement. Earth Surf. Process. Landforms 38, 421–430. https://doi.org/10.1002/esp.3366

Franco, B., Fettweis, X., Lang, C., Erpicum, M., 2012. Impact of spatial resolution on the modelling of the Greenland ice sheet surface mass balance between 1990-2010, using the regional climate model MAR. Cryosph. 6, 695–711. https://doi.org/10.5194/tc-6-695-2012

Giesen, R.H., Andreassen, L.M., Oerlemans, J., van den Broeke, M.R., 2014. Surface energy balance in the ablation zone of Langfjordjøkelen, an arctic, maritime glacier in northern Norway. J. Glaciol. 60, 57–70. https://doi.org/10.3189/2014JoG13J063

Glenn, N.F., Streutker, D.R., Chadwick, D.J., Thackray, G.D., Dorsch, S.J., 2006. Analysis of LiDAR-derived topographic information for characterizing and differentiating landslide morphology and activity. Geomorphology 73, 131–148. https://doi.org/10.1016/j.geomorph.2005.07.006

Gorter, W., van Angelen, J.H., Lenaerts, J.T.M., van den Broeke, M.R., 2014. Present and future near-surface wind climate of Greenland from high resolution regional climate modelling. Clim. Dyn. 42, 1595–1611. https://doi.org/10.1007/s00382-013-1861-2

Hall, D.K., 1988. Assessment of polar climate change using satellite technology. Rev. Geophys. 26, 26. https://doi.org/10.1029/RG026i001p00026

Haubrock, S.N., Kuhnert, M., Chabrillat, S., Güntner, A., Kaufmann, H., 2009. Spatiotemporal variations of soil surface roughness from in-situ laser scanning. Catena 79, 128–139. https://doi.org/10.1016/j.catena.2009.06.005

Hiller, J.K., Smith, M., 2008. Residual relief separation: Digital elevation model enhancement for geomorphological mapping. Earth Surf. Process. Landforms 33, 2266–2276. https://doi.org/10.1002/esp.1659

Hock, R., 2005. Glacier melt: A review of processes and their modelling. Prog. Phys. Geogr. https://doi.org/10.1191/0309133305pp453ra

Hock, R., Holmgren, B., 1996. Some Aspects of Energy Balance and Ablation of Storglaciären. Geogr. Ann. Ser. A, Phys. Geogr. 78, 121–131. https://doi.org/10.1080/04353676.1996.11880458

Hurrell, J.W., Kushnir, Y., Ottersen, G., Visbeck, M., 2003. An overview of the north atlantic oscillation, in: Geophysical Monograph Series. pp. 1–35. https://doi.org/10.1029/134GM01

Immerzeel, W.W., Kraaijenbrink, P.D.A., Shea, J.M., Shrestha, A.B., Pellicciotti, F., Bierkens, M.F.P., de Jong, S.M., 2014. High-resolution monitoring of Himalayan glacier dynamics using unmanned aerial vehicles. Remote Sens. Environ. 150, 93–103. https://doi.org/10.1016/J.RSE.2014.04.025

Irvine-Fynn, T.D.L., Sanz-Ablanedo, E., Rutter, N., Smith, M.W., Chandler, J.H., 2014. Measuring glacier surface roughness using plot-scale, close-range digital photogrammetry. J. Glaciol. 60, 957–969. https://doi.org/10.3189/2014JoG14J032

James, M.R., Robson, S., 2014. Mitigating systematic error in topographic models derived from UAV and ground-based image networks. Earth Surf. Process. Landforms 39, 1413–1420. https://doi.org/10.1002/esp.3609

Jouvet, G., Weidmann, Y., Seguinot, J., Funk, M., Abe, T., Sakakibara, D., Seddik, H., Sugiyama, S., 2017. Initiation of a major calving event on the Bowdoin Glacier captured by UAV photogrammetry. Cryosph. 11, 911–921. https://doi.org/10.5194/tc-11-911-2017

Jouvet, G., Weidmann, Y., van Dongen, E., Lüthi, M.P., Vieli, A., Ryan, J.C., 2019. High-Endurance UAV for Monitoring Calving Glaciers: Application to the Inglefield Bredning and Eqip Sermia, Greenland. Front. Earth Sci. 7. https://doi.org/10.3389/feart.2019.00206

Kljun, N., Calanca, P., Rotach, M.W., Schmid, H.P., 2015. A simple two-dimensional parameterisation for Flux Footprint Prediction (FFP). Geosci. Model Dev. 8, 3695–3713. https://doi.org/10.5194/gmd-8-3695-2015

Kraaijenbrink, P., Meijer, S.W., Shea, J.M., Pellicciotti, F., De Jong, S.M., Immerzeel, W.W., 2016. Seasonal surface velocities of a Himalayan glacier derived by automated correlation of unmanned aerial vehicle imagery. Ann. Glaciol. 57, 103–113. https://doi.org/10.3189/2016AoG71A072

Kuipers Munneke, P., Smeets, C.J.P.P., Reijmer, C.H., Oerlemans, J., van de Wal, R.S.W., van den Broeke, M.R., 2018. The K-transect on the western Greenland Ice Sheet: Surface energy balance (2003–2016). Arctic, Antarct. Alp. Res. 50. https://doi.org/10.1080/15230430.2017.1420952

Kuo, W.L., Steenhuis, T.S., McCulloch, C.E., Mohler, C.L., Weinstein, D.A., DeGloria, S.D., Swaney, D.P., 1999. Effect of grid size on runoff and soil moisture for a variable-source-area hydrology model. Water Resour. Res. 35, 3419–3428. https://doi.org/10.1029/1999WR900183

Lettau, H., 1969. Note on Aerodynamic Roughness-Parameter Estimation on the Basis of Roughness-Element Description. J. Appl. Meteorol. 8, 828–832. https://doi.org/10.1175/1520-0450(1969)008<0828:noarpe>2.0.co;2

Lu, B., He, Y., Liu, H.H.T., 2018. Mapping vegetation biophysical and biochemical properties using unmanned aerial vehicles-acquired imagery. Int. J. Remote Sens. 39, 5265–5287. https://doi.org/10.1080/01431161.2017.1363441

Manfreda, S., McCabe, M.F., Miller, P.E., Lucas, R., Madrigal, V.P., Mallinis, G., Dor, E. Ben, Helman, D., Estes, L., Ciraolo, G., Müllerová, J., Tauro, F., de Lima, M.I., de Lima, J.L.M.P., Maltese, A., Frances, F., Caylor, K., Kohv, M., Perks, M., Ruiz-Pérez, G., Su, Z., Vico, G., Toth, B., 2018. On the use of unmanned aerial systems for environmental monitoring. Remote Sens. https://doi.org/10.3390/rs10040641

Martin, Y., Valeo, C., Tait, M., 2008. Centimetre-scale digital representations of terrain and impacts on depression storage and runoff. Catena 75, 223–233. https://doi.org/10.1016/j.catena.2008.07.005

McCabe, M.F., Aragon, B., Houborg, R., Mascaro, J., 2017. CubeSats in Hydrology: Ultrahigh-Resolution Insights Into Vegetation Dynamics and Terrestrial Evaporation. Water Resour. Res. 53, 10017–10024. https://doi.org/10.1002/2017WR022240@10.1002/(ISSN)1944-9208.COMHES1

Miles, E.S., Steiner, J.F., Brun, F., 2017. Highly variable aerodynamic roughness length (z0) for a hummocky debris-covered glacier. J. Geophys. Res. Atmos. 122, 8447–8466. https://doi.org/10.1002/2017JD026510

Mouginot, J., Rignot, E., BjØrk, A.A., van den Broeke, M.R., Millan, R., Morlighem, M., Noël, B., Scheuchl, B., Wood, M., 2019. Forty-six years of Greenland Ice Sheet mass balance from 1972 to 2018. Proc. Natl. Acad. Sci. U. S. A. 116, 9239–9244. https://doi.org/10.7280/D1MM37

Munro, D.S., 1989. Surface roughness and bulk heat transfer on a glacier: comparison with eddy correlation. J. Glaciol. 35, 343–348. https://doi.org/10.1017/S0022143000009266

Neff, W., Compo, G.P., Ralph, F.M., Shupe, M.D., 2014. Continental heat anomalies and the extreme melting of the Greenland ice surface in 2012 and 1889. J. Geophys. Res. 119, 6520–6536. https://doi.org/10.1002/2014JD021470

Neumann, T.A., Martino, A.J., Markus, T., Bae, S., Bock, M.R., Brenner, A.C., Brunt, K.M., Cavanaugh, J., Fernandes, S.T., Hancock, D.W., Harbeck, K., Lee, J., Kurtz, N.T., Luers, P.J., Luthcke, S.B.,

Magruder, L., Pennington, T.A., Ramos-Izquierdo, L., Rebold, T., Skoog, J., Thomas, T.C., 2019. The Ice, Cloud, and Land Elevation Satellite – 2 mission: A global geolocated photon product derived from the Advanced Topographic Laser Altimeter System. Remote Sens. Environ. 233, 111325. https://doi.org/10.1016/j.rse.2019.111325

Nghiem, S. V., Hall, D.K., Mote, T.L., Tedesco, M., Albert, M.R., Keegan, K., Shuman, C.A., DiGirolamo, N.E., Neumann, G., 2012. The extreme melt across the Greenland ice sheet in 2012. Geophys. Res. Lett. 39, 2012GL053611. https://doi.org/10.1029/2012GL053611

Nick, F.M., Vieli, A., Andersen, M.L., Joughin, I., Payne, A., Edwards, T.L., Pattyn, F., van de Wal, R.S.W., 2013. Future sea-level rise from Greenland's main outlet glaciers in a warming climate. Nature 497, 235–238. https://doi.org/10.1038/nature12068

Nield, J.M., King, J., Wiggs, G.F.S., Leyland, J., Bryant, R.G., Chiverrell, R.C., Darby, S.E., Eckardt, F.D., Thomas, D.S.G., Vircavs, L.H., Washington, R., 2013. Estimating aerodynamic roughness over complex surface terrain. J. Geophys. Res. Atmos. 118, 12,948-12,961. https://doi.org/10.1002/2013JD020632

Nield, J.M., Wiggs, G.F.S., Squirrell, R.S., 2011. Aeolian sand strip mobility and protodune development on a drying beach: Examining surface moisture and surface roughness patterns measured by terrestrial laser scanning. Earth Surf. Process. Landforms 36, 513–522. https://doi.org/10.1002/esp.2071

Noël, B., van de Berg, W.J., van Meijgaard, E., Kuipers Munneke, P., van de Wal, R.S.W., van den Broeke, M.R., 2015. Evaluation of the updated regional climate model RACMO2.3: Summer snowfall impact on the Greenland Ice Sheet. Cryosph. 9, 1831–1844. https://doi.org/10.5194/tc-9-1831-2015

Oerlemans, J., Vugts, H.F., 1993. A meteorological experiment in the melting zone of the Greenland ice sheet. Bull. - Am. Meteorol. Soc. 74, 355–365. https://doi.org/10.1175/1520-0477(1993)074<0355:AMEITM>2.0.CO;2

Oltmanns, M., Straneo, F., Tedesco, M., 2019. Increased Greenland melt triggered by large-scale, year-round cyclonic moisture intrusions. Cryosph. 13, 815–825. https://doi.org/10.5194/tc-13-815-2019

P P Smeets, C.J., van den Broeke, M.R., 2008. Temporal and Spatial Variations of the Aerodynamic Roughness Length in the Ablation Zone of the Greenland Ice Sheet 128, 315–338. https://doi.org/10.1007/s10546-008-9291-0

Radić, V., Menounos, B., Shea, J., Fitzpatrick, N., Tessema, M.A., Déry, S.J., 2017. Evaluation of different methods to model near-surface turbulent fluxes for a mountain glacier in the Cariboo Mountains, BC, Canada. Cryosphere 11, 2897–2918. https://doi.org/10.5194/tc-11-2897-2017

Rees, W.G., Arnold, N.S., 2006. Scale-dependent roughness of a glacier surface: Implications for radar backscatter and aerodynamic roughness modelling. J. Glaciol. 52, 214–222. https://doi.org/10.3189/172756506781828665

Rodríguez-Caballero, E., Cantón, Y., Chamizo, S., Afana, A., Solé-Benet, A., 2012. Effects of biological soil crusts on surface roughness and implications for runoff and erosion. Geomorphology 145–146, 81–89. https://doi.org/10.1016/j.geomorph.2011.12.042

Rounce, D.R., Quincey, D.J., McKinney, D.C., 2015a. Debris-covered energy balance model for Imja-Lhotse Shar Glacier in the Everest region of Nepal. Cryosph. Discuss. 9, 3503–3540. https://doi.org/10.5194/tcd-9-3503-2015

Rounce, D.R., Quincey, D.J., McKinney, D.C., 2015b. Debris-covered glacier energy balance model for

Imja-Lhotse Shar Glacier in the Everest region of Nepal. Cryosphere 9, 2295–2310. https://doi.org/10.5194/tc-9-2295-2015

Ryan, J.C., Hubbard, A., Stibal, M., Irvine-Fynn, T.D., Cook, J., Smith, L.C., Cameron, K., Box, J., 2018. Dark zone of the Greenland Ice Sheet controlled by distributed biologically-active impurities. Nat. Commun. 9. https://doi.org/10.1038/s41467-018-03353-2

Ryan, J.C., Hubbard, A.L., Box, J.E., Todd, J., Christoffersen, P., Carr, J.R., Holt, T.O., Snooke, N., 2015. UAV photogrammetry and structure from motion to assess calving dynamics at Store Glacier, a large outlet draining the Greenland ice sheet. Cryosphere 9, 1–11. https://doi.org/10.5194/tc-9-1-2015

Sasgen, I., van den Broeke, M., Bamber, J.L., Rignot, E., Sørensen, L.S., Wouters, B., Martinec, Z., Velicogna, I., Simonsen, S.B., 2012. Timing and origin of recent regional ice-mass loss in Greenland. Earth Planet. Sci. Lett. https://doi.org/10.1016/j.epsl.2012.03.033

Schuenemann, K.C., Cassano, J.J., 2010. Changes in synoptic weather patterns and Greenland precipitation in the 20th and 21st centuries: 2. Analysis of 21st century atmospheric changes using self-organizing maps. J. Geophys. Res. Atmos. 115, 5108. https://doi.org/10.1029/2009JD011706

Sicart, J.E., Litt, M., Helgason, W., Tahar, V. Ben, Chaperon, T., 2014. A study of the atmospheric surface layer and roughness lengths on the high-altitude tropical Zongo glacier, Bolivia. J. Geophys. Res. Atmos. 119, 3793–3808. https://doi.org/10.1002/2013JD020615

Smeets, C.J.P.P., Broeke, M.R., 2008. Temporal and spatial variations of the aerodynamic roughness length in the ablation zone of the greenland ice sheet. Boundary-Layer Meteorol. 128, 315–338. https://doi.org/10.1007/s10546-008-9291-0

Smeets, C.J.P.P., Duynkerke, P.G., Vugts, H.F., 1999. Observed wind profiles and turbulence fluxes over an ice surface with changing surface roughness. Boundary-Layer Meteorol. 92, 101–123. https://doi.org/10.1023/a:1001899015849

Smeets, C.J.P.P., Duynkerke, P.G., Vugts, H.F., 1998. Turbulence characteristics of the stable boundary layer over a mid-latitude glacier. Part I: a combination of katabatic and large-scale forcing. Boundary-Layer Meteorol. 87, 117–145. https://doi.org/10.1023/A:1000860406093

Smith, B.E., Raymond, C.F., Scambos, T., 2006. Anisotropic texture of ice sheet surfaces. J. Geophys. Res. Earth Surf. 111. https://doi.org/10.1029/2005JF000393

Smith, M.W., 2014. Roughness in the Earth Sciences. Earth-Science Rev. https://doi.org/10.1016/j.earscirev.2014.05.016

Smith, M.W., Quincey, D.J., Dixon, T., Bingham, R.G., Carrivick, J.L., Irvine-Fynn, T.D.L., Rippin, D.M., 2016. Aerodynamic roughness of glacial ice surfaces derived from high-resolution topographic data. J. Geophys. Res. F Earth Surf. 121, 748–766. https://doi.org/10.1002/2015JF003759

Snavely, N., 2011. Scene Reconstruction and Visualization from Internet Photo Collections: A Survey. IPSJ Trans. Comput. Vis. Appl. 3, 44–66. https://doi.org/10.2197/ipsjtcva.3.44

Teng, G.E., Zhou, M., Li, C.R., Wu, H.H., Li, W., Meng, F.R., Zhou, C.C., Ma, L., 2017. Mini-UAV LIDAR for power line inspection, in: International Archives of the Photogrammetry, Remote Sensing and Spatial Information Sciences - ISPRS Archives. pp. 297–300. https://doi.org/10.5194/isprs-archives-XLII-2-W7-297-2017

van Angelen, J.H., van den Broeke, M.R., Wouters, B., Lenaerts, J.T.M., 2014. Contemporary (1960–2012) Evolution of the Climate and Surface Mass Balance of the Greenland Ice Sheet. Surv.

Geophys. 35, 1155–1174. https://doi.org/10.1007/s10712-013-9261-z

van den Broeke, M.R., Bamber, J.L., Ettema, J., Rignot, E., Schrama, E., van Berg, W.J. De, van Meijgaard, E., Velicogna, I., Wouters, B., 2009. Partitioning recent Greenland mass loss. Science (80-.). 326, 984–986. https://doi.org/10.1126/science.1178176

van den Broeke, M.R., Box, J., Fettweis, X., Hanna, E., Noël, B., Tedesco, M., van As, D., van de Berg, W.J., van Kampenhout, L., 2017. Greenland Ice Sheet Surface Mass Loss: Recent Developments in Observation and Modeling. Curr. Clim. Chang. Reports. https://doi.org/10.1007/s40641-017-0084-8

van den Broeke, M.R., Enderlin, E.M., Howat, I.M., Kuipers Munneke, P., Noël, B.P.Y., Jan Van De Berg, W., van Meijgaard, E., Wouters, B., 2016. On the recent contribution of the Greenland ice sheet to sea level change. Cryosph. 10, 1933–1946. https://doi.org/10.5194/tc-10-1933-2016

van der Wal, T., Abma, B., Viguria, A., Prévinaire, E., Zarco-Tejada, P.J., Serruys, P., van Valkengoed, E., van der Voet, P., 2013. Fieldcopter: Unmanned aerial systems for crop monitoring services, in: Precision Agriculture 2013 - Papers Presented at the 9th European Conference on Precision Agriculture, ECPA 2013. pp. 169–175.

Vavrus, S.J., 2013. Extreme Arctic cyclones in CMIP5 historical simulations. Geophys. Res. Lett. 40, 6208–6212. https://doi.org/10.1002/2013GL058161

Verhoeven, G., 2011. Taking computer vision aloft - archaeological three-dimensional reconstructions from aerial photographs with photoscan. Archaeol. Prospect. https://doi.org/10.1002/arp.399

Watanabe, E., Wang, J., Sumi, A., Hasumi, H., 2006. Arctic dipole anomaly and its contribution to sea ice export from the Arctic Ocean in the 20th century. Geophys. Res. Lett. 33, L23703. https://doi.org/10.1029/2006GL028112

Westoby, M.J., Brasington, J., Glasser, N.F., Hambrey, M.J., Reynolds, J.M., 2012. 'Structure-from-Motion' photogrammetry: A low-cost, effective tool for geoscience applications. Geomorphology 179, 300–314. https://doi.org/10.1016/j.geomorph.2012.08.021

Wouters, B., Bamber, J.L., van den Broeke, M.R., Lenaerts, J.T.M., Sasgen, I., 2013. Limits in detecting acceleration of ice sheet mass loss due to climate variability. Nat. Geosci. 6, 613–616. https://doi.org/10.1038/ngeo1874

Wüst, S., Wendt, V., Linz, R., Bittner, M., 2017. Smoothing data series by means of cubic splines: quality of approximation and introduction of a repeating spline approach. Atmos. Meas. Tech 10, 3453–3462. https://doi.org/10.5194/amt-10-3453-2017

Zhao, L., Hou, R., Wu, F., 2020. Effect of DEM grid size on microrelief indexes estimation for sloping lands after reservoir tillage. Soil Tillage Res. 196. https://doi.org/10.1016/j.still.2019.104451

Appendix I: Abbreviations

AWS	Automatic Weather Station
DEM	Digital Elevation Model
DOF	Degree of Freedom
FG	Fixed Grid
GCP	Ground Control Point
GNSS	Global Navigation Satellite System
GNSS-AT	Global Navigation Satellite System Aerial Triangulation
GrIS	Greenland Ice Sheet
IMAU	Institute for Marine and Atmospheric research Utrecht
MF	Moving Footprint
RCM	Regional Climate Model
RPAS	Remotely Piloted Aircraft System
SLR	Sea-level rise